remote sensing

MDPI

Article

High-Resolution Precipitation Modeling in Complex Terrains Using Hybrid Interpolation Techniques: Incorporating Physiographic and MODIS Cloud Cover Influences

Karam Alsafadi [1], Shuoben Bi [1,*], Bashar Bashir [2], Ehsan Sharifi [3], Abdullah Alsalman [2], Amit Kumar [4] and Shamsuddin Shahid [5]

[1] School of Geographical Sciences, Nanjing University of Information Science and Technology, Nanjing 210044, China; 200040@nuist.edu.cn
[2] Department of Civil Engineering, College of Engineering, King Saud University, P.O. Box 800, Riyadh 11421, Saudi Arabia
[3] Department of Computational Hydrosystems, Helmholtz Centre for Environmental Research—UFZ, 04318 Leipzig, Germany
[4] School of Hydrology and Water Resources, Nanjing University of Information Science and Technology, Nanjing 210044, China
[5] Department of Water & Environmental Engineering, Faculty of Civil Engineering, Universiti Teknologi Malaysia, Skudai 81310, Johor, Malaysia
* Correspondence: bishuoben@nuist.edu.cn

Abstract: The inclusion of physiographic and atmospheric influences is critical for spatial modeling of orographic precipitation in complex terrains. However, attempts to incorporate cloud cover frequency (CCF) data when interpolating precipitation are limited. CCF considers the rain shadow effect during interpolation to avoid an overly strong relationship between elevation and precipitation in areas at equivalent altitudes across rain shadows. Conventional multivariate regression or geostatistical methods assume the precipitation–explanatory variable relationship to be steady, even though this relation is often non-stationarity in complex terrains. This study proposed a novel spatial mapping approach for precipitation that combines regression-kriging (RK) to leverage its advantages over conventional multivariate regression and the spatial autocorrelation structure of residuals via kriging. The proposed hybrid model, RK (GT + CCF), utilized CCF and other physiographic factors to enhance the accuracy of precipitation interpolation. The implementation of this approach was examined in a mountainous region of southern Syria using in situ monthly precipitation data from 57 rain gauges. The RK model's performance was compared with conventional multivariate regression models (CMRMs) that used geographical and topographical (GT) factors and CCF as predictors. The results indicated that the RK model outperformed the CMRMs with a root mean square error of <8 mm, a mean absolute percentage error range of 5–15%, and an R^2 range of 0.75–0.96. The findings of this study showed that the incorporation of MODIS–CCF with physiographic variables as covariates significantly improved the interpolation accuracy by 5–20%, with the largest improvement in modeling precipitation in March.

Keywords: regression-kriging; geostatistical methods; regional climate modeling; MODIS cloud; orographic effectiveness; Syria

check for updates

Citation: Alsafadi, K.; Bi, S.; Bashir, B.; Sharifi, E.; Alsalman, A.; Kumar, A.; Shahid, S. High-Resolution Precipitation Modeling in Complex Terrains Using Hybrid Interpolation Techniques: Incorporating Physiographic and MODIS Cloud Cover Influences. *Remote Sens.* **2023**, *15*, 2435. https://doi.org/10.3390/rs15092435

Academic Editors: Yanping Li, Ya Huang, Omer Yetemen and Qing Yang

Received: 25 March 2023
Revised: 28 April 2023
Accepted: 2 May 2023
Published: 5 May 2023

Copyright: © 2023 by the authors. Licensee MDPI, Basel, Switzerland. This article is an open access article distributed under the terms and conditions of the Creative Commons Attribution (CC BY) license (https://creativecommons.org/licenses/by/4.0/).

1. Introduction

Spatial datasets for precipitation at a high spatial resolution are essential for environmental monitoring, agricultural planning [1], rainforest studies [2], hydrological modeling [3,4], and other sectors [5]. However, obtaining such datasets can be challenging due to limited precipitation observation stations, especially in mountainous areas having complex terrains [6,7]. The spatial variability of precipitation over complex terrains is highly heterogeneous. Precipitation may occur within a few kilometers around a gauge, whereas there is

no precipitation at a short distance. Thus, spatial interpolation of precipitation is a major challenge in such an area. Global datasets often fail to represent local precipitation patterns accurately [8,9]. They are also mostly available at a low spatial resolution [10,11], except for some recent products [12–15]. Therefore, it is necessary to develop accurate methods for estimating precipitation to a sufficient spatial resolution before using them in hydrological models or related applications. However, developing high-resolution precipitation data is always challenging, particularly for complex terrains.

In recent years, two types of methods are frequently used for developing high-spatial-resolution precipitation data with a specific horizontal spacing from observation data: the first includes interpolation techniques based on sparse in situ observations [16–19], and the second involves downscaling coarse-resolution gridded datasets, such as via the use of reanalysis, numerical weather models (NWM), regional climate models (RCMs), and remotely sensed data, to fine spatial resolution [20–23]. The downscaling approach based on RCMs or NWMs employs physical processes of the coupled land-and-atmosphere systems, which need a large dataset from different sources [24]. Such an approach is also time-consuming and computationally cumbersome [25–28]. Therefore, spatial interpolation techniques are more widely used to estimate precipitation distribution over an area [29,30].

Spatial interpolation techniques based on in situ observation can be divided into five subtypes: (i) geostatistical, (ii) deterministic, (iii) multiple regression, (iv) machine learning, and (v) hybrid methods. The geostatistical methods include simple kriging (SK), universal kriging (UK), ordinary kriging (OK), co-kriging (CK), and kriging with an external trend (KED) [31]. Among them, OK only considers the spatial autocorrelations of the sampled points and presumes that their structural constituents are locally stationary and stochastic in space. In contrast, UK, CK, and KED describe the effects of the explanatory variables on the dependent factor and use the spatial autocorrelation of the predicted variable. The deterministic methods include Thiessen polygons, inverse distance weighting (IDW), and radial basis function, which assume that nearby factors affect the predicted surface more than distant factors [32]. Many studies have compared the performance of these precipitation spatial modeling methods [33–35]. Theoretically, KED and CK are considered better than OK at interpolating precipitation spatial variability as they also consider the effects of explanatory factors. However, the superior performance of these two algorithms over OK is still subject to a multitude of factors, such as precipitation type, the strength of the relationship between precipitation and explanatory factors, the density of rain gauges, and so on [36,37].

The third subtype of spatial interpolation techniques is multivariate regression (MR), where a linear or nonlinear regression is fitted between precipitation and the predictive variables to interpolate precipitation at ungauged locations [6,38]. The ordinary least squares (OLS) approach is generally used for fitting the regression line. The OLS approach assumes that precipitation and predictive variables are associated in large-scale regression fitting in a stationary form, and the resulting model's residuals follow a normal distribution [39–41]. However, these assumptions are not valid in most cases. As a result, novel MR approaches, such as generalized additive model (GAM) [42], geographically weighted regression (GWR) [43,44], and geographically and temporally weighted regression [45], have been introduced for spatial interpolation of precipitation. These three MR models significantly outperform OLS in modeling hypotheses and regression fitting. They can more accurately explain the geographically nonlinear or nonstationary responses between precipitation and related explanatory factors [41]. These regression approaches are also simple and computationally less expensive.

Nevertheless, as the relationship among precipitation-related variables is not always linear, nonlinear regression methods, such as machine learning and artificial intelligence approaches, have shown efficiency in precipitation interpolation [46]. These methods include artificial neural network (ANN) [47], self-organizing map (SOM), multilayer perceptron (MLP) [48], fuzzy inference [49], and random forest [50–52]. However, it is not yet clear which method provides the most reliable precipitation estimates [9]. Nevertheless,

several studies have indicated that a single method (e.g., geostatistical, linear regression, or machine learning) might not be able to explain precipitation occurrence properly, especially when modeling local precipitation patterns in complex terrains. Therefore, hybrid interpolation methods are proposed over typical interpolation approaches for complex terrains, especially when focusing on extreme precipitation events [27,28]. Hybrid interpolation methods combine several types of algorithms. Therefore, they are more capable of reproducing the observed precipitation at a high spatial resolution more precisely than a single method [53–57]. In general, hybrid interpolation employs one approach to estimate the target variable first and then another approach to interpolate the residuals of the first approach. Finally, the partial interpolation of the two methods is combined. Some examples of hybrid interpolation methods are Auto-Searched Orographic and Atmospheric Effects Detrended Kriging (ASOADeK) [58,59]; regression-kriging (RK), which combines the OLS method and OK [60,61]; geographically weighted regression kriging (GWRK); local regression-kriging (LRK) [62]; geographically and temporally weighted regression kriging (GTWRK) [56]; and stratified geographically weighted regression-residual kriging (s-GWRK) [41]. In addition to the above methods, some studies developed new hybrid interpolation methods by combining the deterministic/geostatistical methods and machine learning algorithms, such as regression-kriging and neural network residual kriging (RKNNRK) [63]; model tree (MT) and kriging method [64,65]; and coupling random forest (RF) and inverse distance weighting (RF-IDW) [66].

Recently, auxiliary data have been used as independent variables for interpolation [67]. For example, steep precipitation gradients are correlated with atmospheric and orographic factors, geographic position, altitudes, slopes, and coastline distance. However, covariates should be available at fine resolution for high-resolution interpolation of precipitation. Covariates are generally climate variables derived from climate/satellite models/products [68–70]. Other covariates are topography-related variables, such as elevation and slope. Several studies used topography and normalized difference vegetation index (NDVI) as covariate/auxiliary variables available in high resolution [71–73]. These environmental factors, obtained from fine-resolution satellite datasets, are closely related to rainfall only in arid and semiarid regions where rainfall patterns are affected by elevation [71]. Additionally, timescale is important when selecting covariates/auxiliary data. For instance, when using a covariate that represents the greenness of an ecosystem's surface and shows the vegetation in a particular region, the response of the greenness indicator to a precipitation event lags in the order of a few months or weeks [74].

One of the high-resolution covariates with a strong relationship with precipitation is cloud cover and its characteristics. It can be derived from satellites to improve the spatial resolution of precipitation fields [22]. There is no precipitation if there are no clouds, and increased cloud cover frequency (CCF) also increases precipitation occurrences [75–77]. This study presents an improved method by integrating mathematical tools with spatial interpolation techniques (multivariate regression with residual correction) to generate high-resolution continuous precipitation surfaces. Furthermore, this study investigates the interaction between a climatic component (precipitation) and independent climatic factors (topographical and geographical variables), as well as the capacity of these variables to explain the spatial variance in monthly precipitation. Thus, the main objective of this research is to integrate conventional multivariate regression and spatial autocorrelation structure of residuals using kriging to improve the accuracy of precipitation interpolation, employing remotely sensed data, such as the MODIS (Moderate Resolution Imaging Spectroradiometer) cloud cover and other physiographic factors.

2. Materials and Methods

2.1. Study Area and Data Collection

This study was carried out in one of the mountainous regions in southwestern Syria and northern Jordan, which is situated between latitudes of 32°17′45″ N and 33°25′01″ N, and longitudes of 35°47′30″ E and 37°30′45″ E, with a catchment area of

20,362.2 km^2 (Figure 1). The study area is characterized by a continental climate with a wet-cold climate in the winter and a dry-hot climate in the summer. The average summer temperature varies between 18 and 32 °C in July, while the winter average varies between 3 and 10 °C in January. The regional mean annual precipitation is 283 mm (the 25th and 75th percentiles are 200 and 350 mm, respectively), with a maximum rainfall of roughly 470 mm (1982–2015) [78]. The mean annual CCF is 20–55%, with the highest value of 40–95% in February (2000–2015). According to the Köppen–Geiger classification, the region is located in the temperate-wet climatic zone in the central and western hilly regions. In contrast, the climate is desert (arid climate) and continental or steppe (semi-arid climate) toward the east [78]. The region is classified into three physiographic units: (i) mountain region in the western and central area (Mount Hermon and Jabal Al Arab), (ii) plateau in the northwestern part (Golan Heights extent), and (iii) a plain area that occupies most of the study area (Horan plain) with an altitude varying between -18 in the southwest (lower part of the Yarmouk river) and 2814 m above mean sea level (m asl) in the northwest (Mount Hermon or Jabal El Sheikh).

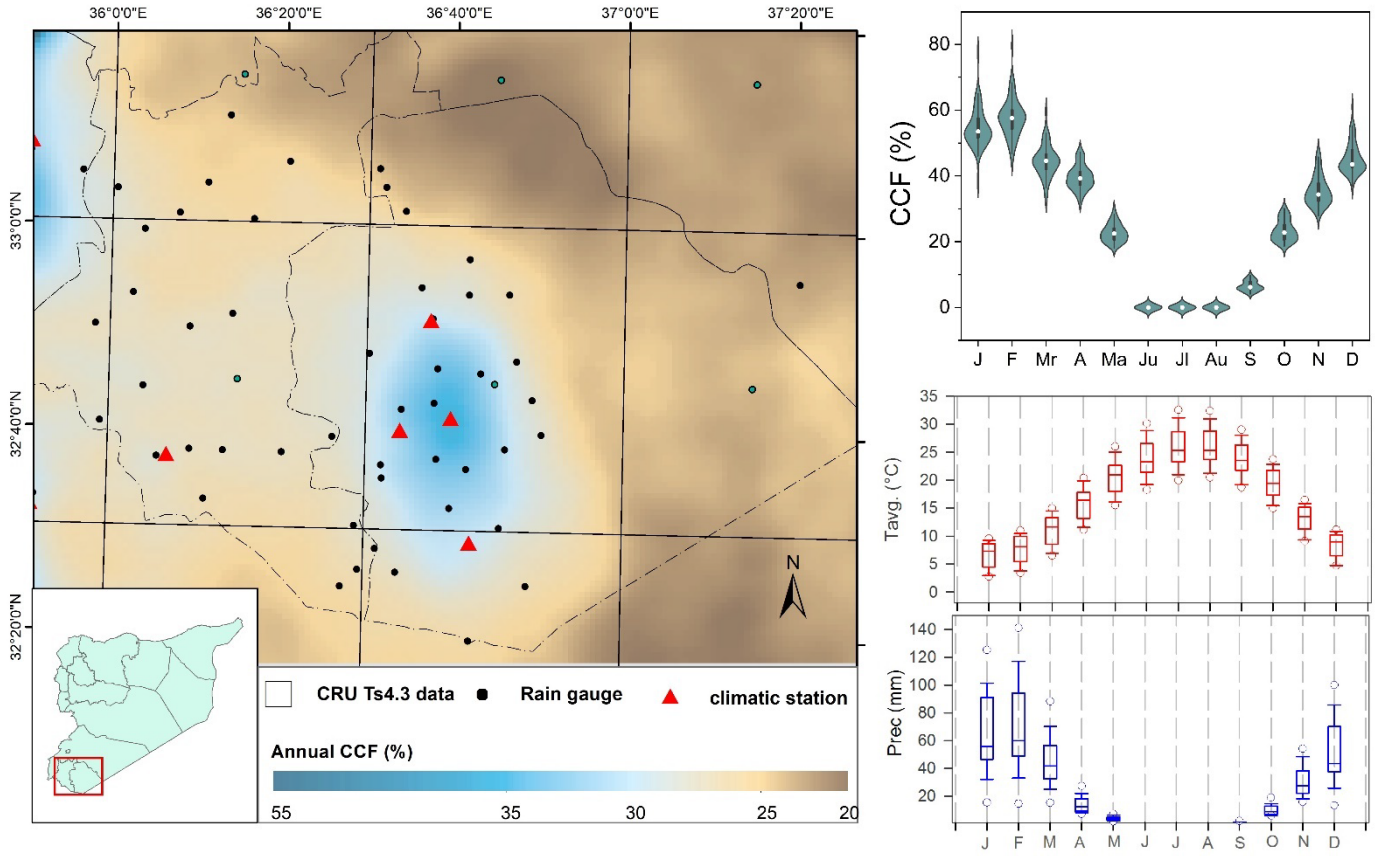


Figure 1. The location of the study area, the regional seasonal cycle of precipitation (mm.), the average temperature (°C) for the 1982–2015 period, and the average cloud cover frequencies (CCF, %) for the 2000–2015 period.

In this study, the spatial modeling of precipitation at fine resolution was based on in situ and remotely sensed data from several sources, which are summarized in the following sub-sections.

2.1.1. Monthly Observed Precipitation Data

The in situ observation data from 57 rain gauges were collected from the databases of the Syrian Meteorological Authority (SMA), the Syrian Ministry of Agriculture and Agrarian Reform (SMOAAR), and the Jordan Meteorological Department (JMD). The stations were selected considering their locations in areas that vary topographically and

geographically, as shown in Table 1 and Figure 1, where all these data were collected on a monthly time scale for 1984–2015. The stations with observations for at least 20 years were only included in the data preparation stage. The gridded precipitation data from the CRU Ts4.3 dataset [11] with a resolution of 0.5° were used as the reference for correction, gap filling, and homogeneity testing, which led to interruption-free data acquisition. Table 2 shows the precipitation datasets used in modeling and validation.

Table 1. Details of observed monthly precipitation data used in modeling and validation.

Variable	Data Type	Number of Stations/Points	Spatial Resolution	Reference Period	Source
Observed precipitation (mm)	Rain gauge and climatic stations (Historical)	57	–	1984–2015	SMA SMOAAR JMD
CRU Ts4.3 precipitation (mm)	Gridded data (Historical)	9 gridded points	0.5 degree	1984–2015	https://crudata.uea.ac.uk/cru/data/hrg/, (accessed on 7 September 2022)
TerraClimate precipitation (mm)	Gridded data (Monthly average)	–	~4 km (2.5 arc. min)	1970–2000	https://www.climatologylab.org/, (accessed on 7 September 2022)
WorldClim V. 2.1 precipitation (mm)	Gridded data (Monthly average)	–	~1 km (30 arc-second)	1981–2010	https://www.worldclim.org/, (accessed on 7 September 2022)
CHELSA V1.0 precipitation (mm)	Gridded data (Monthly average)	–	~1 km (30 arc-second)	1979–2016	https://chelsa-climate.org/, (accessed on 7 September 2022)

2.1.2. Auxiliary Remote Sensing Data

To produce a regional high-spatial-resolution (at ~1 km resolution) precipitation dataset accurately, auxiliary variables with the same horizontal spacing should be obtained. The elevation data for the study area were calculated and extracted for the in situ stations and the whole area from the Digital Elevation Model (DEM) obtained from the US Geological Survey's Center for Earth Resources Observation and Science (EROS) Archive-Digital Elevation—Global (GTOPO30) within the HYDRO1k project data with a horizontal grid spacing of 30 arc-second (approx. ~1 km) resolution (Figure 2) (https://earthexplorer.usgs.gov, (accessed on 7 September 2022)).

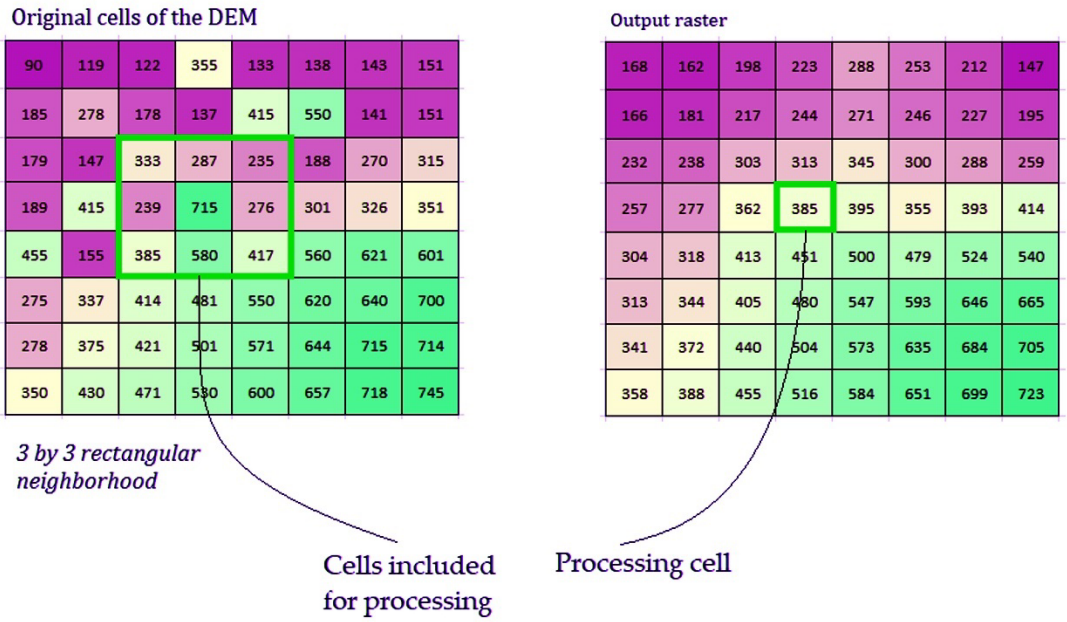


Figure 2. Rectangular neighborhood method using height and width (3 by 3) to determine the new value of each elevation/CCF cell.

The cloud cover data (at ~1 km resolution) were extracted from the 16-year MODIS satellite data (2000–2015). The MODIS CCF data have a twice-a-day frequency [79]. The CCF product used in this study was extracted from the original daily data of the daytime surface reflectance products from both TERRA (i.e., MOD09GA, which compiled at approx. 10:30 a.m. local time) and AQUA (i.e., MYD09GA at approx. 1:30 p.m.) from February 2000 to March 2014 (see Wilson et al. [79] for more details).

Table 2. Details of remote sensing data used.

Dataset	Variable	Period	Spatial Resolution	Temporal Scale	Reference
Global Cloud Cover MODIS	Cloud frequency (%)	2000–2015	1 km	Monthly	[79]
HYDRO1K (GTOPO30)	Digital Elevation Model	–	~1 km (30 arc-second)	Monthly	[80]

2.2. Data Analysis

2.2.1. Preliminary Analysis of Monthly Precipitation Series

Precipitation data require careful preparation and handling, including outlier removal, selection of the candidate and reference stations, data gap filling, and homogeneity testing, regardless of the spatial interpolation method used. These matters are important when employing data from several sources with different settings. As a result, the data series were subjected to a precise procedure to ensure data completeness, homogeneity, and filling of data gaps for reliable climate evaluation. To that end, data quality was assessed by analyzing the difference in the monthly series between candidate and neighboring stations (i.e., pairwise comparisons) and interpolating missing values using the regression line (OLS method) (see Alsafadi et al. [57] for more details). The gridded precipitation data from the CRU Ts4.3 dataset were also used when overlaps in the missing values were evident among the precipitation series, which ultimately led to interruption-free data acquisition. Additionally, the standard normal homogeneity test (SNHT) was applied [81] to assess data homogeneity. More information on the quality control and homogeneity test processes can be found in the AnClim software, version 5.016 documentation [82].

2.2.2. Preprocessing of Explanatory Variables

The independent factors were chosen from the most frequently referenced geo-climatic parameters in the literature [83,84], considering their availability and relationships with precipitation in the study. Elevation (Elv.) and latitude (Lat.) are most widely used in terms of their impact on precipitation [84–86]. Elevation information takes into consideration the environmental lapse rate (ELR), i.e., the ratio of change in precipitation with altitude variation, or orographic precipitation (OP) [87,88]. The longitude (Lon.) position and the distance to a sea coastline (Cdist) represent continentality, which significantly affects precipitation. The distance to a coast is an important geographic factor since it represents the influence of marine wind and its inland movement. Other components with a significant relationship with precipitation are cloud formation, cloud properties, and CCF. However, they are rarely employed since they are not always available [89,90]. CCF considers the rain shadow effect, which leads to the redistribution of precipitation forced by the local complex terrain. In the study area, the interpolation of precipitation is difficult due to the highly contrasting local climates and low rain gauge density [37]. Given these restrictions, previous studies confirmed the need to add CCF with terrain influences to avoid an overly strong relationship between elevation and precipitation with rain gauges at equivalent altitudes across rain shadows [13,17] Other topographic variables that may affect cloud formation and wind fluxes, such as aspects and slope, were not used in this study due to their low relationship with precipitation in the study area and were replaced by the CCF effect.

The selected covariables were preprocessed employing several methods. The DEM data were smoothed by removing or reducing the spatial variation (i.e., small-scale noise removal) to detect the ideal orographic effect of elevation [84]. An average of adjacent pixel values at 2 km, 3 km, and 5 km distances were considered to determine the ideal DEM with a strong relationship with precipitation. For this purpose, this study employed the focal statistics tool of ArcMap v.10.8 (Esri. Redlands, CA, USA) and the rectangular neighborhood method with a given height and width. Since the original resolution of the

DEM was 1 km, we determined the new value of each cell as a square with the height and width of the 2, 3, and 5 nearest input pixels, respectively (Figure 2). Next, the relationship between precipitation and the new smoothed elevation points was determined to adapt the optimal DEM (the ideal topographic effectiveness) [21,57].

The principal component analysis (PCA) is often used to reveal the structure and composition of the relationship between independent variables based on the existence of a correlation between them (*r* correlation > 0.33) [91]. The PCA method helps evaluate the interrelationships between groups of correlated variables. It may be useful to convert the original dataset of variables into new uncorrelated variables called the principal components (PCs). These new PCs are derived in descending order of importance; for example, PC1 represents the highest variance from the original data, PC2 represents the second highest variance, and so on [92]. As such, the PCA method reduces the number of variables without a substantial loss in the total explained variance. It is a procedure that helps avoid multicollinearity among independent variables and, thus, the difficulty of obtaining an optimal model that should explain the best variance ratio for the studied dependent variable [93,94]. In this study, the principal components of four factors affecting the spatial distribution of precipitation were analyzed: latitude, longitude, elevation, and distance to the sea coastline. In addition to the smoothed monthly CCF data, the grid data—a total of 27,813 dot cells—was used for the PCA. The PCA was calculated using SPSS v. 26, (IBM Corp. Armonk, NY, USA) and the PCs that accounted for at least 90% of the total variance were considered.

2.2.3. Fine-Scale Modeling Using Regression-Kriging (RK)

RK is a local hybrid interpolation technique which merges conventional multivariate regression model (CMRM) and OK [60,61] to obtain spatially more accurate predictions of precipitation. In RK, the CMRM's residuals (i.e., unexplained variation) are handled as random bias and interpolated using a kriging algorithm. The components of RK are expressed as follows:

$$\overline{Z}(s_0) = \sum_{k=0}^{p} \beta_k\,(s_0)\,X_k\,(s_0) + \sum_{i=1}^{n} \omega_i\,\varepsilon(s_i) \quad (1)$$

where $\overline{Z}(s_0)$ is the estimation at site s_0; $\beta_k\,(s_0)$ is the CMRM coefficient at site s_0; $X_k\,(s_0)$ is the variable (PC score) at site s_0; p is the overall variable applied in the CMRM model; ω_i is the kriging weight; $\varepsilon(s_i)$ is the CMRM residual at observed station s_i; and *n* is the range of neighboring points for local modeling. The first portion of the left side of the equation represents the CMRM, and the second portion indicates the kriging of the MRM residuals.

Local RK is established to consider the local relationship between a target variable and covariates as a replacement for applying a single regression function for an entire observed dataset, which is used to handle spatial non-stationarity [57,62]. Herein, we used all the stations for the RK process due to the small number of stations as well as the short spatial dimensions of the study area.

2.2.4. Steps Involved in Fitting, Calculating, and Assessing the CMRM and RK Models

The RK process for estimating monthly precipitation in the study is summarized below:

Step 1: Fitting a CMRM function to specific stations to express the relationship between observed precipitation and the independent variables, i.e., the extracted PC scores from the PCA and the significant independent variables xn in the CMRM using the stepwise regression method (SW). The CMRM is expressed in Equations (2) and (3):

$$Y(s_0), SW = \beta 0 + \beta 1\,x1 + \beta 2\,x2 + \beta 3\,x3 + \ldots \beta n\,xn \quad (2)$$

$$Y(s_0),\ PCs = \beta 0 + \beta 1\,PC1 + \beta 2\,PC2 + \beta 3\,PC3 + \ldots \beta n\,PCn \quad (3)$$

Step 2: Setting the CMRM function to the independent variables (PC scores' layers) at each gridded point to obtain a potential estimate of the precipitation variable (potential surfaces). The MRM coefficients β_k are predicted by fitting the OLS regression line [95]. The OLS estimator chooses the best model that matches the input data and minimizes the sum of the square error as much as possible. Therefore, it takes the equation using matrices as follows:

$$\hat{\beta}\ \text{ols} = \left(\text{X}\,\acute{\text{X}}\right)^{-1}\text{X}\underline{\acute{\text{Y}}} \tag{4}$$

Step 3: Computing the residual values of the monthly precipitation models (i.e., unexplained variation), which are the differences between the predicted values from the CMRM surfaces and the observed values $\overline{o}$ from the stations: $\varepsilon(s_i) = \overline{o}(s_0) - \ Y(s_0)$.

Step 4: Calculating the empirical semi-variogram of the CMRM's residuals of monthly precipitation as a measure of the variation between the CMRM's residuals calculated based on the following equation [33]:

$$\gamma_{(h)} = \frac{1}{2N(h)}\sum_{i=1}^{N(h)}\{Z(x_i) - Z(x_i + h)\}^2 \tag{5}$$

where $\gamma_{(h)}$ is the semi-variance; $N(h)$ is the number of pairs of data locations separated by the spatial lag h; $Z(x_i)$ is the CMRM's residuals of the variable x_i at site *i*; and $Z(x_i + h)$ is the MRM's residuals of the variable distributed at distance *h* from x_i. As such, the empirical semi-variogram is calculated as 1/2 of the averaged squared difference between the components of point pairs.

Step 5: Using an exponential variogram model to fit the computed empirical semi-variogram and predicted range "a" (correlated distance parameter), partial sill variance "C1" (the pure variance of the point), and nugget "c0" (uncorrelated or random noise). The exponential variogram model is the most fitted because it provides the best result for the residual correction of the CMRM functions, i.e., unexplained variation of CMRM fitting, to obtain climatic surfaces over Syria [57] and another region [8]. The exponential variogram model is expressed in Equation (6):

$$\Gamma_{(h)} = c0 + C1\left[1 - \exp\left(\frac{-h}{a}\right)\right] \tag{6}$$

where h denotes the distance between the predicted location and the observed location. The model parameters are then optimized. The model parameters, nugget, partial sill, and other(s) are optimized using cross-validation, focusing on estimating the range parameter.

Step 6: Predicting the residual values of monthly precipitation at the gridded points using the previously fitted exponential variogram model.

Step 7: Ultimately, merging the potential surfaces of monthly precipitation estimates and the kriged residual surfaces of monthly precipitation estimates as the prediction of the final surface. Correspondingly, the sum of the CMRM variance and the kriging variance is considered the prediction variance, as shown in Figure 3. Various schemes have been tested for modeling monthly precipitation. We categorized them into three models, as shown in Table 3, each with a clear objective.

Step 8: In this last step, the leave-one-out cross-validation (LOOCV) is performed using statistical indicators, root mean square error (RMSE), mean absolute percentage error (MAPE), coefficient of determination (R^2), and Pearson's correlation coefficient (r) [57,85,96].

Table 3. Description of models applied for modeling monthly precipitation.

Model	Description	Included Variables	Benefits
Regression model: CMRM-SW (GT)	Fitting the CMRM function using the stepwise regression (SW) method.	Both geographical and topographical factors (elevation, longitude, latitude, and distance to the coast) by including only significant independent variables.	Calculating geographical and topographical contribution (GT) in precipitation modeling.
Regression model: CMRM-PCs (GT+ CCF)	Using the extracted PC scores from the PCA to fit the CMRM function.	Geographical and topographical factors (elevation, longitude, latitude, and distance to the coast) were included, besides the CCF data. The extracted PC scores from the PCA.	Calculating remotely sensed CCF contribution in precipitation modeling besides GT effects.
Hybrid model: RK (GT + CCF)	Using the extracted PC scores from the PCA to fit the CMRM function and then adding the CMRM's residuals using OK with exponential variogram model.	As presented in the CMRM-PC (GT + CCF) scheme.	CMRM's residual correction to improve the outputs.

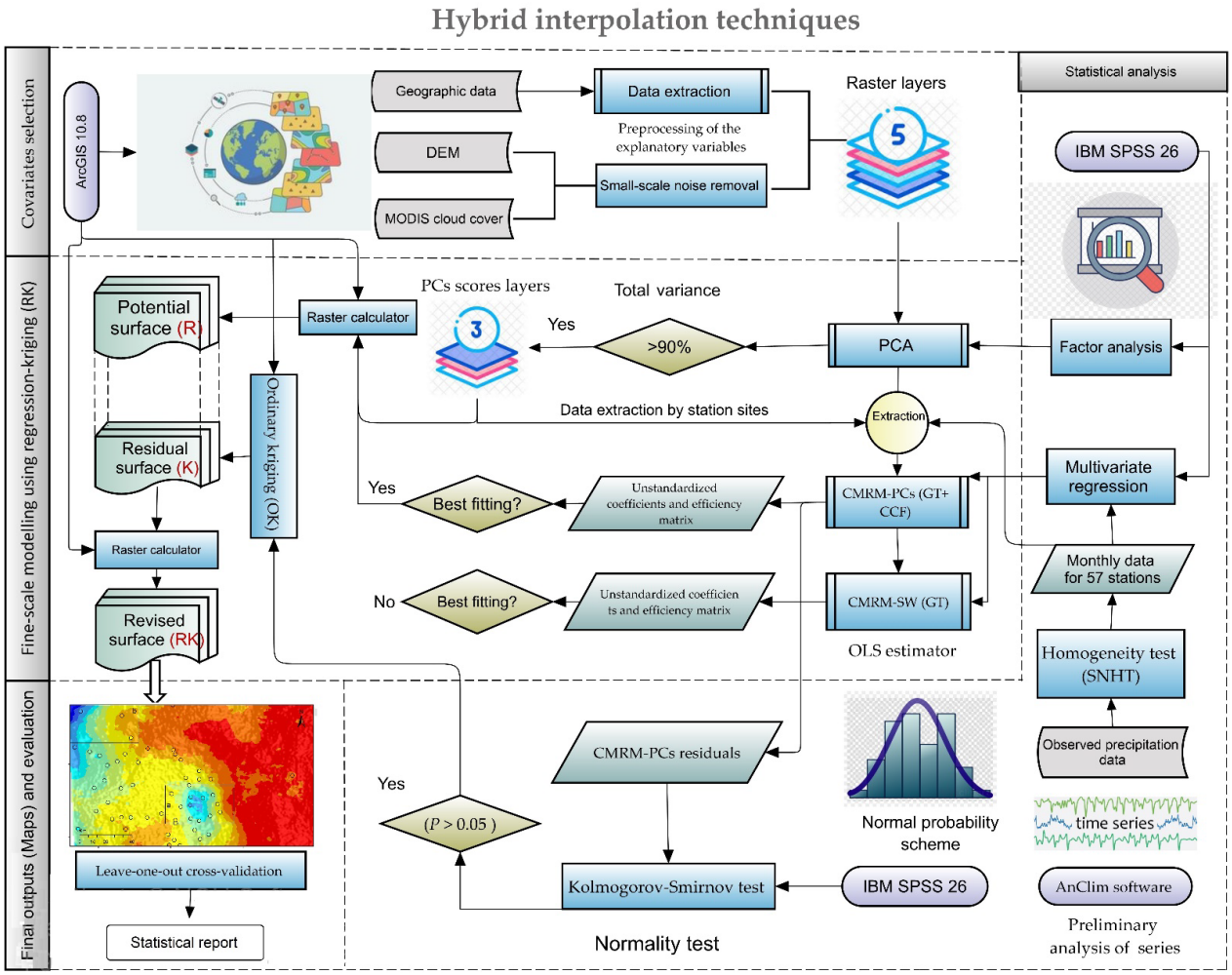


Figure 3. Flowchart of the methodology of fitting, calculating, and assessing the CMRM and RK models.

3. Results

3.1. Effect of Topographical–Geographical Factors on the Spatial Variability of Precipitation

The small-scale DEM noise removal procedure revealed the optimal effects on monthly precipitation patterns for the horizontal scale of 3 km (Figure 4, the right panel). The highest correlation between monthly precipitation and altitude was in March (r = 0.51, $p < 0.05$), which was a significant positive correlation, while the lowest value of correlation was in September (r = 0.3, $p < 0.05$). In the case of the continentality effect, the longitude location

(Lon.) and distance to the seacoast (Cdist.) showed a significant negative correlation with monthly precipitation. The highest values of the negative correlations between monthly precipitation and (Lon.)/(Cdist) were for November and December (r = −0.36 to −0.42, p < 0.05), while the lowest (negative correlation) was for March and May, with a value of −0.2.

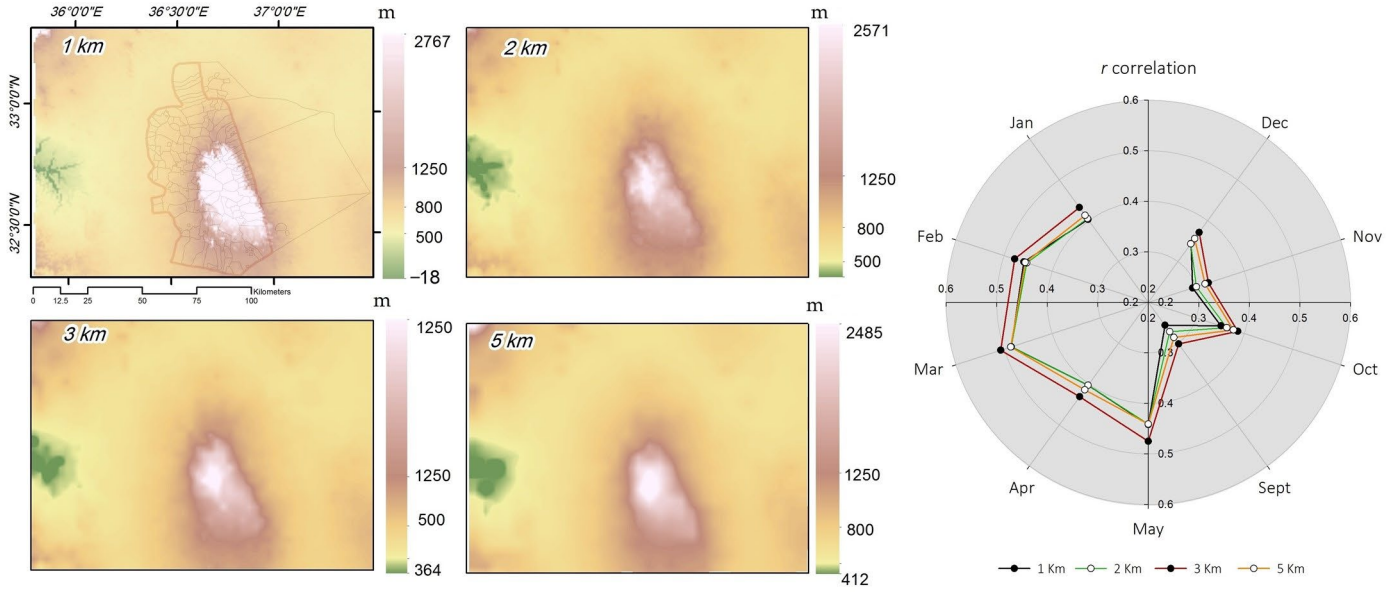


Figure 4. The spatial correlation between elevation using smoothed DEMs at multiple horizontal scales (e.g., 1, 2, 3, and 5 km) and average monthly precipitation.

3.2. Spatial Distribution of CCF and Its Effect on the Average Monthly Precipitation

Figure 5 shows the spatial distribution of monthly CCF. The highest CCF was in winter, with 40–95% in January and February, and 34–82% in December. The high CCF (>70%) was in the mountainous regions of Jabal Alarab and Aljulan Heights in the winter, while the lowest was in September (3.5–25%). Interestingly, regardless of the monthly CCF amounts, its distribution is spatially symmetric, making it a good predictor of spatial precipitation patterns in complex terrains.

Because CCF considers the rain shadow effect, which leads to the redistribution of precipitation forced by the local complex terrain, we analyzed the spatial correlation between the CCFs at multiple horizontal scales and the observed average monthly precipitation. The optimal MODIS-CCF surface effects on monthly precipitation patterns were the most significant at a horizontal scale of 7 km. Figure 5 shows the correlation between the observed monthly precipitation and the monthly CCF, ranging between 0.58 and 0.84. The highest values were in April and March (r > 0.8, p < 0.05), with a significantly positive correlation, while the lowest was in September (r = 0.58, p < 0.05), but it was also statistically significant. This indicates that CCF is a good predictor for explaining complex terrain precipitation patterns and can improve interpolation accuracy.

3.3. Interrelationships between Explanatory Variables and PC Analysis

Before performing the PCA, the structure and composition of the interrelationships between the independent variables contributing to the precipitation variance should be revealed under autocorrelation (r correlation > 0.33) and multicollinearity assumptions regarding the independent variables. The results indicate that the monthly CCF is negatively correlated with longitudes (<−0.5) for all months except September through November and May. The same pattern exists for the "distance to the seacoast". On the other hand, the monthly CCF and elevation are positively correlated, with values ranging from 0.35 to 0.53 for January through May and at the annual level (Figure 6a). The correlation matrix

of monthly CCF (Figure 6b) reveals significant positive interrelationships between the monthly CCFs of January, February, March, and April, which take a spatially homogeneous pattern with an *r* ranging between 0.84 and 0.92. A similar interrelationship was observed between the average annual CCF and the CCFs for January through April, with an *r* higher than 0.9. The results indicate that PCA is required to convert the correlated covariables into uncorrelated variables (PCs).

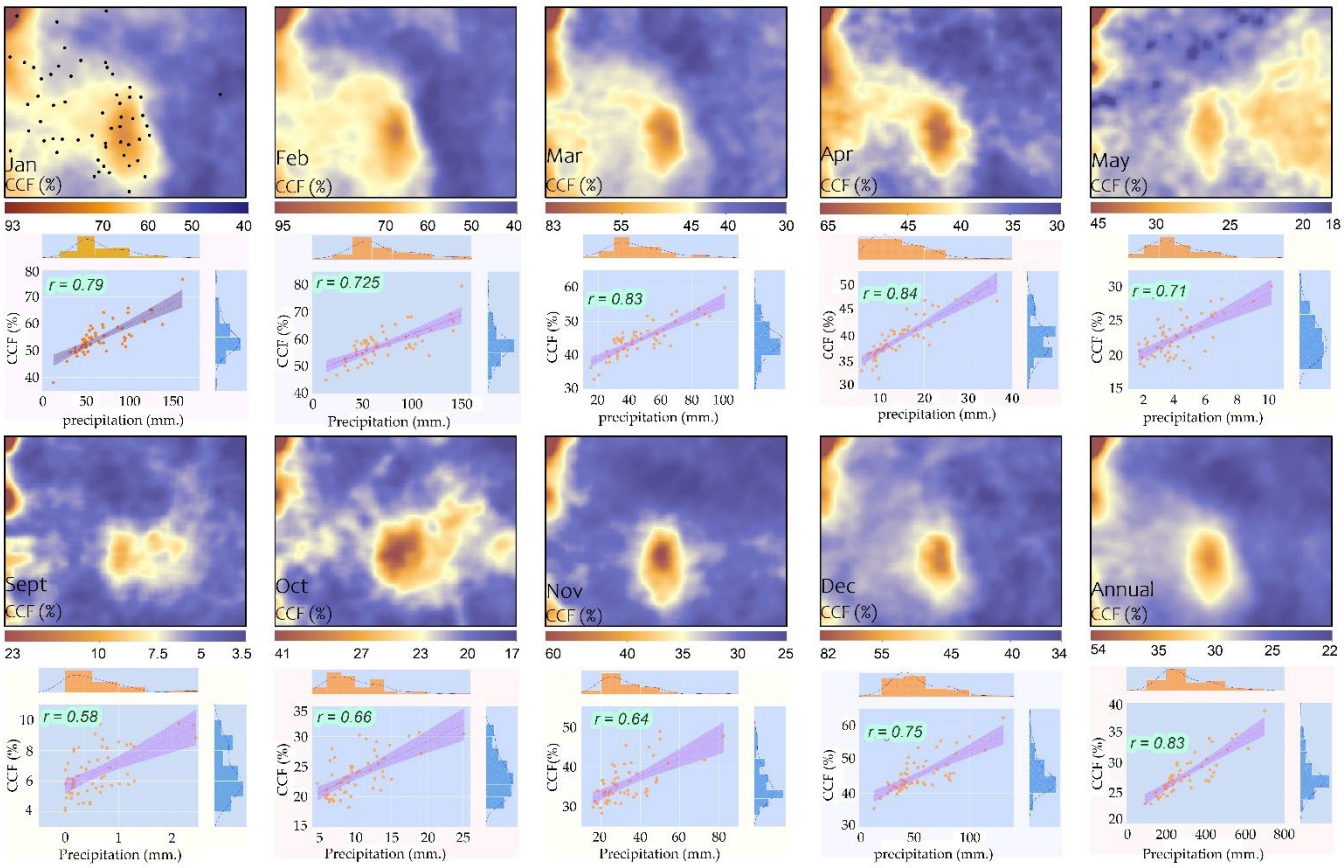


Figure 5. The spatial distribution of smoothed monthly CCF (%) at a 7 km horizontal scale and its correlation with observed average monthly precipitation at 57 rain gauges.

The PCA of the explanatory variables were used to extract the key factors contributing to the spatial variability of precipitation on the monthly and annual scales (Figure 7). The extraction of the key factors employing the rotation method resulted in three main PCs. The first component (PC1) in all months explains the highest variance in the included factors, with values ranging between 39% and 49.5%, while the PC3 contributes the least to spatial variance, ranging between 18% and 23% of the total variance. The explained cumulative variance for the extracted PCs ranges between 90% for September and 97.1% for January (Figure 7a). Figure 7b shows the loadings of the original variables on the extracted PCs after rotation. The "longitudes" and "distance to the seacoast" are positively loaded on the PC1 (0.94 to 0.99).

It is worth noting that the CCF is negatively and partly loaded on the same component, with a value ranging from −0.66 to −0.78. The inverse correlation indicates decreased CCF with the distance from the seacoast in January, February, March, April, and December, as well as the average annual value. In contrast, the CCF in May is partly loaded positively on the PC1 due to increased CCF when moving away from the seacoast (see Figure 5).

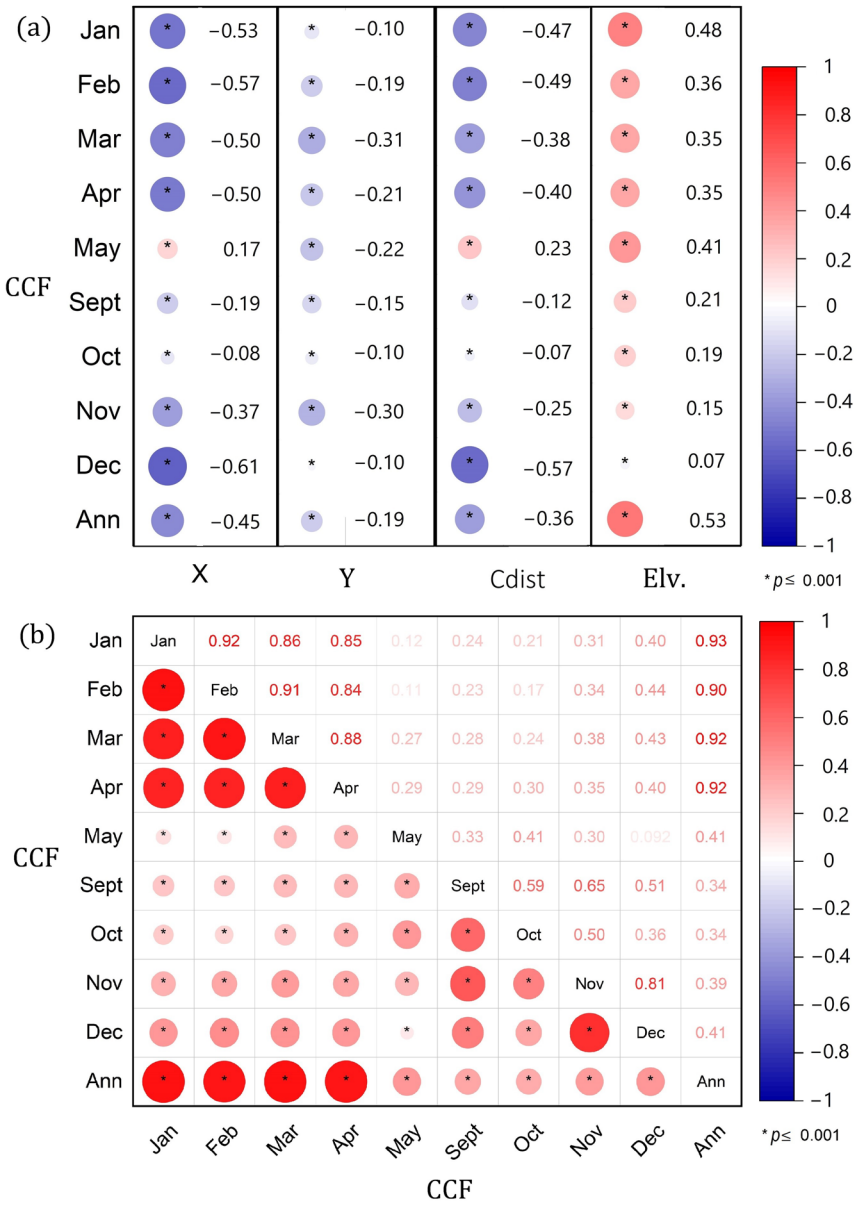


Figure 6. Correlation matrices between the explanatory variables: (**a**) the topographical–geographical factors with the monthly CCF, and (**b**) correlation matrix of monthly CCFs.

The CCF is positively loaded on the PC2 in all months, except March and December, with a value ranging between 0.44 and 0.88. This positive loading of CCF is accompanied by the elevation factor, which is also positively loaded on the PC2 in all months, with a value ranging between 0.81 and 0.97. This indicates that an increase in elevation increases the CCF. Table 4 shows the correlation matrix between the observed precipitation and extracted PCs after the varimax rotation method.

Table 4. Eigenvectors of the correlation matrix between the observed monthly precipitation (n = 57) and extracted PCs after varimax rotation method with Kaiser normalization.

PCs/Prc.	January	February	March	April	May	June	July	August	September	October	November	December	Annual
PC1	−0.415	−0.39	−0.38	−0.45	−0.35	–	–	–	−0.34	−0.30	−0.36	−0.42	−0.36
PC2	0.47	0.51	0.005	0.49	0.64	–	–	–	0.12	0.55	0.46	0.46	0.55
PC3	0.14	0.13	0.56	0.13	0.30	–	–	–	0.27	0.34	0.33	0.17	0.17

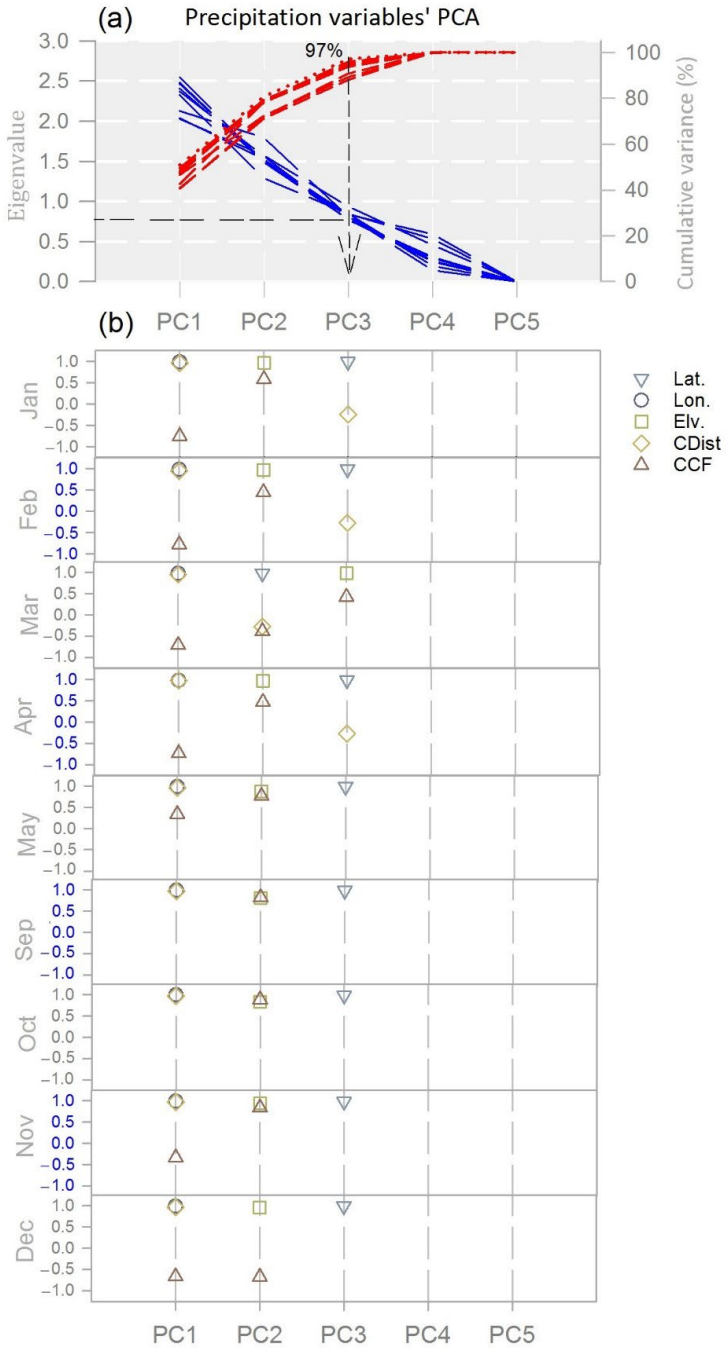


Figure 7. A scree plot presenting the cumulative variance (%) for the extracted PCs (**a**) and the loading matrix of the explanatory variables on the PCs (**b**).

3.4. Modeling of Monthly Precipitation Using the CMRM

The CMRM process referred to above was applied to the region, which covers a complex terrain with two CMRM schemes. The first CMRMs-SW (GT) scheme was fitted to ensure that the CMRM's efficiency is only related to the ability of the geographical–topographical factors to interpret the spatial variability of precipitation. It was carried out after selecting the best independent variables based on their significant effect on the spatial variability of precipitation, i.e., using the SW regression method and excluding variables that have no effect. The second CMRMs-PCA (GT + CCF) scheme was fitted to ensure that the CMRM's efficiency is related to the ability of the GT factors and CCF to interpret the spatial variability of precipitation. It was conducted after obtaining the three main PCs that

explain the highest variance instead of applying the SW method to add the CCF variable to avoid multicollinearity.

Table 5 reveals that the applied CMRMs-SW (GT) on a monthly scale has statistical significance based on the adjusted determination coefficient (Adj. R^2) and standard error. This indicates that the geographical–topographical factors influence the spatial variation of monthly precipitation. The interpretation of the statistical significance of the factors demonstrates high adequacy in explicating the monthly precipitation patterns in the complex topography, specifically in the winter months (Dec, Jan, and Feb), with an Adj. R^2 of 0.71, 0.70, and 0.66, respectively, whereas the precipitation patterns are well interpreted for the remaining months, with an Adj. R^2 ranging from 0.42 to 0.61.

Table 5. Unstandardized coefficients of the CMRMs-SW (GT) used (β) to estimate average monthly precipitation and some statistical indicators to assess the models' performance (the GT effect-based potential precipitation surfaces using the SW method).

Variables	β	January	February	March	April	May	June	July	August	September	October	November	December
Constant	β_0	3303	3013	1706	600	4.8	–	–	–	51.1	13.5	44.9	2610
Elv.	β_1	0.083	0.088	0.053	0.017	0.005	–	–	–	0.001	0.010	0.025	0.064
Lon.	β_2	−85.4	−83	−46.9	−16.5	–	–	–	–	−1.42	–	–	−71.8
Lat.	β_3	–	–	–	–	–	–	–	–	–	–	–	–
CDist.	β_4	–	–	–	–	–0.04	–	–	–	–	−0.10	−0.28	–
r correlation		0.84	0.81	0.79	0.77	0.73	–	–	–	0.69	0.75	0.65	0.843
Adj. R^2		0.70	0.66	0.61	0.6	0.53	–	–	–	0.46	0.56	0.42	0.71
RMSE (mm.)		16.25	18.4	11.8	4.1	1.25	–	–	–	0.42	2.6	10.2	13.3
Sig. value (*p*)		<0.01	<0.01	<0.01	<0.01	<0.01	–	–	–	<0.01	<0.01	<0.01	<0.01

The CCF was included to improve the accuracy of the CMRM outputs in the study area. This helps avoid an excessive relationship between altitude and precipitation in areas at equivalent altitudes across rain shadows. The results shown in Table 6 reveal that the applied CMRMs-PCA (GT + CCF) on a monthly scale has statistical significance based on the Adj. R^2 and that the CCF has an obvious influence on the spatial variation of monthly precipitation besides the geographical–topographical factors. The CCF demonstrates high performance in improving the CMRMs' outputs, specifically during spring (March, April, and May), with an Adj. R^2 of 0.83, 0.72, and 0.73, respectively. Additionally, the spatial precipitation patterns are exceedingly interpreted in December, January, and February, with an Adj. R^2 of 0.78, 0.781, and 0.77, respectively. Once the CMRMs-PCA (GT + CCF) method was used instead of the CMRMs-SW (GT), the standard error of the estimation became lower.

Table 6. Unstandardized coefficients of the CMRMs-PCA (GT + CCF) used to estimate average monthly precipitation and the statistical indicators to assess the models' performance (i.e., the GT and CCF effect-based potential precipitation surfaces using the PCA).

Variables	β	January	February	March	April	May	June	July	August	September	October	November	December
Constant	β_0	33.4	36.6	26.2	8.05	2.8	–	–	–	0.18	6.8	23.7	28
PC1	β_1	−37.7	−37.4	−21.5	−9.6	−1.62	–	–	–	−0.47	−3.6	−11	−29.1
PC2	β_2	18.8	18.9	2.02	3.54	1.03	–	–	–	0.31	2.35	6.74	15.3
PC3	β_3	−0.09	1.1	12.3	0.13	0.14	–	–	–	−0.01	0.42	1.9	−1.6
r correlation		0.885	0.88	0.91	0.85	0.856	–	–	–	0.72	0.82	0.76	0.88
Adj. R^2		0.781	0.77	0.83	0.72	0.73	–	–	–	0.51	0.67	0.53	0.78
RMSE (mm.)		14.37	15.7	8.3	3.5	0.98	–	–	–	0.42	2.4	9.0	11.8
Sig. value (*p*)		<0.01	<0.01	<0.01	<0.01	<0.01	–	–	–	<0.01	<0.01	<0.01	<0.01

3.5. Interpolation of the CMRM's Residuals

Figure 8 presents the monthly CMRMs-PCA (GT + CCF) residual diagnostics for the observed data. The outputs of the normality test, as shown in Figure 8, show that most of the diagnostics are normally distributed based on the Kolmogorov–Smirnov test (K-S test) or the null hypothesis, which assumes that the residuals are taken from a normal distributed

form, with $p > 0.05$ for all months except September. In other words, the significance value of each CMRM's residual distribution is greater than 0.05 and the null hypothesis is accepted; the majority of the expected cumulative probability of the standardized residual data yielded by the CMRMs is aligned along the 45-degree line of the residuals, analogous to a normal probability scheme (normal P–P plot). This indicates that the selected models' residuals are normally distributed and can be interpolated using a geostatistical method, such as OK.

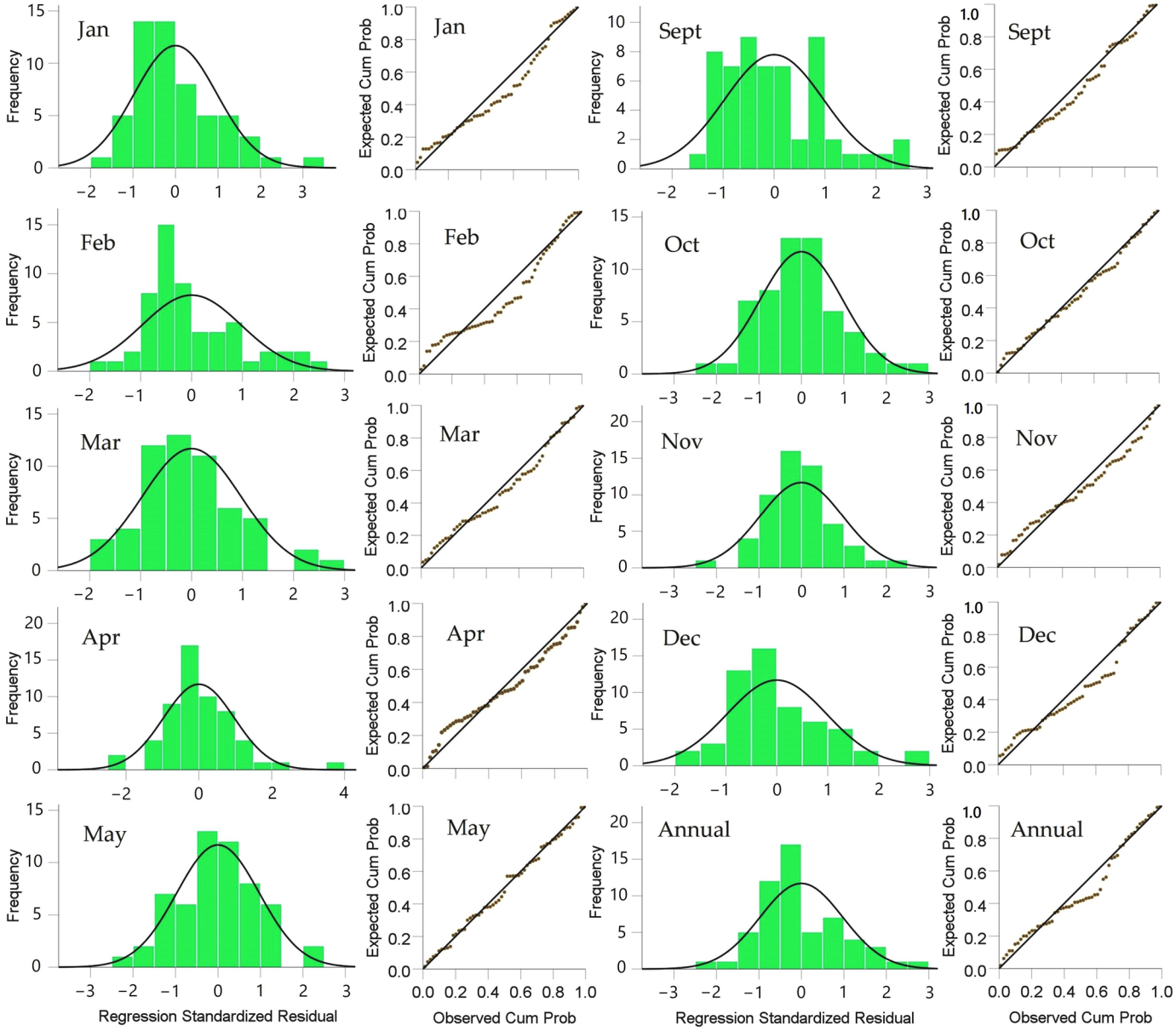


Figure 8. Histograms of CMRMs-PCA (GT + CCF) standardized residual distribution and normal P–P plots of CMRMs-PCA (GT + CCF) standardized residual.

Figure 9 shows that most of the CMRM residual values are between ±15 and ±20 mm for the winter months, at ±10 for March and November, and at ±50 for the mean annual total precipitation using the OK method. The values present a nearly monolithic pattern where the highest residuals recede in limited ranges. For instance, there are positive residuals in the central, western, and eastern areas and negative residuals in the northern and southern parts. All these residual surfaces show approximate agreement with the distribution patterns. Thus, these modeled surfaces were used to adjust the potential

surfaces (i.e., CMRM surfaces) to obtain a reliable estimate of the spatial variability of monthly precipitation.

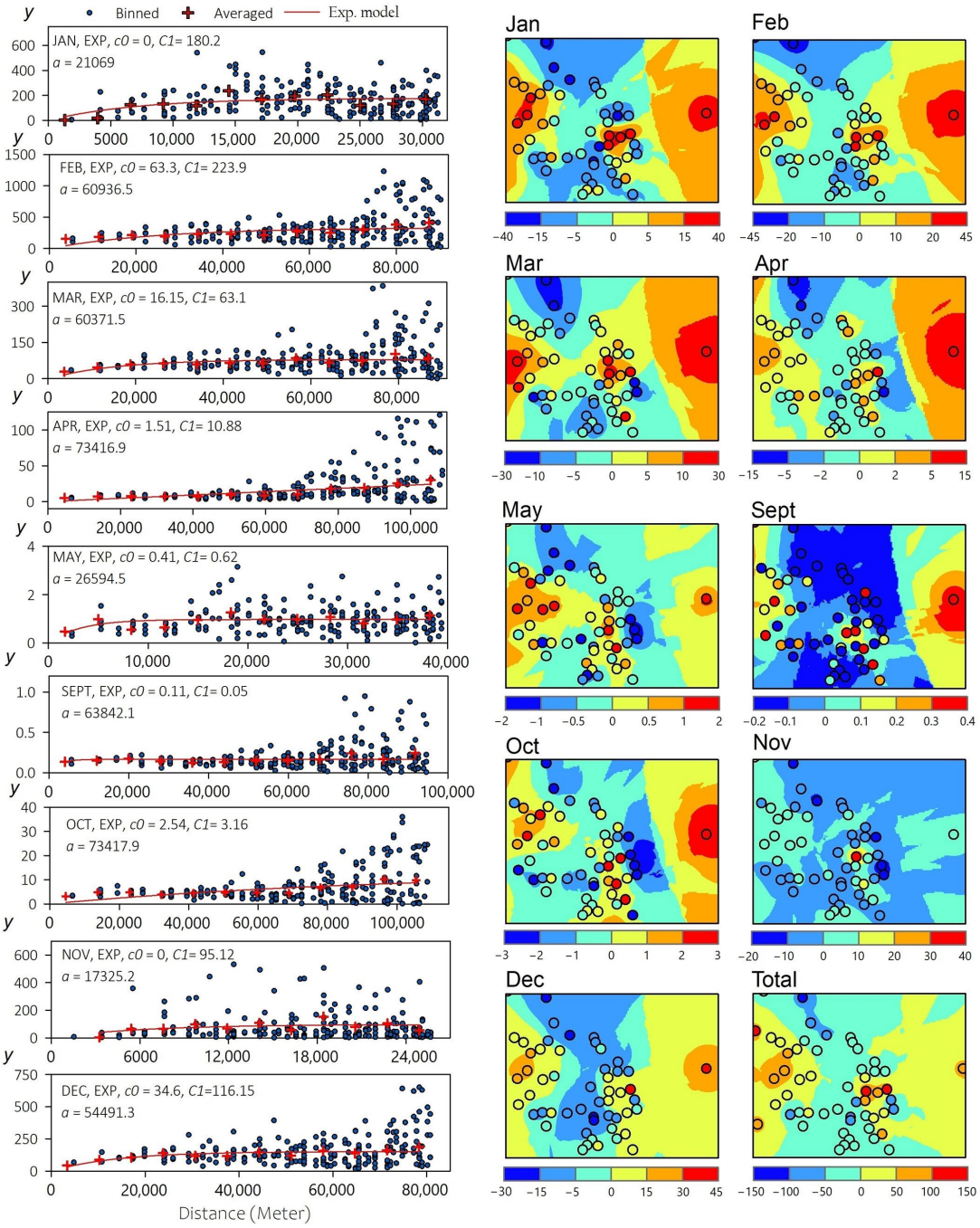


Figure 9. Spatial distribution of CMRMs-PCA (GT + CCF) residuals using the OK method (right maps), and the empirical semi-variogram of the CMRM's residuals and its fitting using the exponential variogram (Exp.) model (left panels).

3.6. Performance of CMRMs and RK Models in the Prediction of Precipitation

The RK's performance was compared to the CMRMs that used geographical and topographical (GT) factors as predictors and the CMRMs that incorporated the GT and CCF influences. The model validation indicated that the RK (GT + CCF) outperformed the single methods with an RMSE of <8 mm, a MAPE range of 5–15%, and an R^2 range of 0.75–0.96. The present study showed that the GT variables explained 42–70% of the

total spatial variance in precipitation. Incorporating CCF as a covariate significantly improved the interpolation accuracy by 5–20%, with the biggest improvement in the March, May, and April models, respectively. On the other hand, the kriging of the CMRMs' residuals significantly improved the interpolation accuracy by 12–28%, with the biggest improvements in the November, October, and April models, respectively (Figure 10).

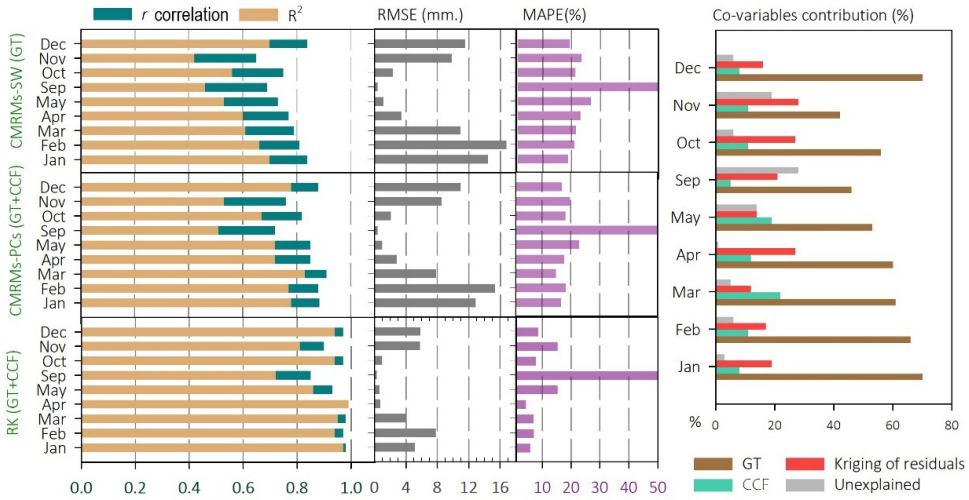


Figure 10. Assessment of the CMRMs versus the RK model in the prediction of monthly precipitation (*r* correlation, R^2, MAPE, and RMSE), and the covariables' contribution to improving the RK model's accuracy (right panel).

Figure 11 shows the scatter plots of the observed monthly precipitation against the predicted precipitation for all months. The plots reveal more consistent prediction using the hybrid (RK) model, with an R^2 of 0.9 and 0.993 for monthly and annual precipitation, respectively. This confirms that the hybrid method outperforms the single methods and that the CCF significantly improves the interpolation accuracy for all months and at the annual scale. Figure 12 shows the final monthly precipitation distribution using the RK method.

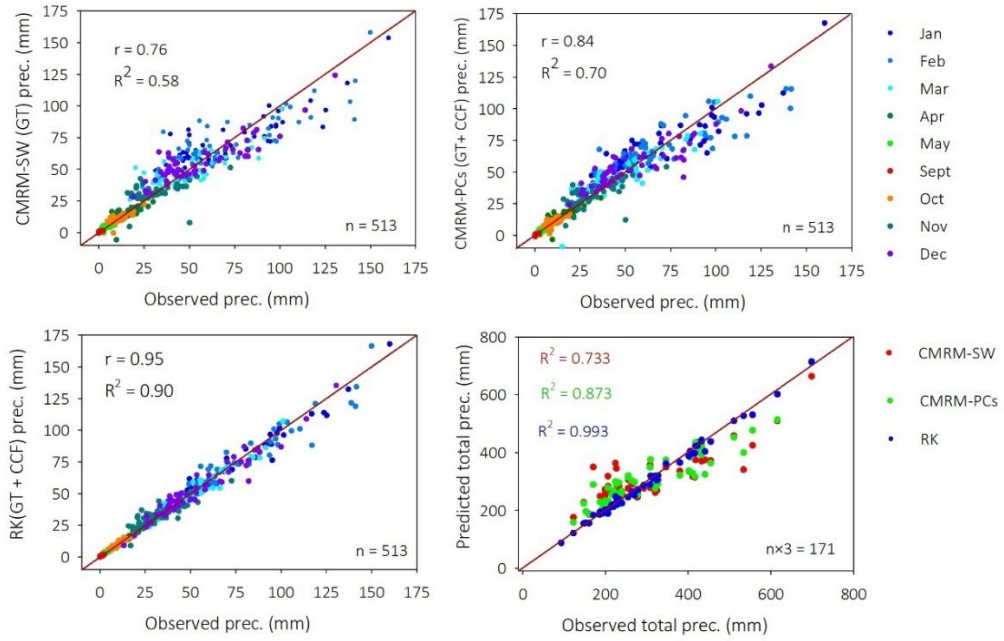


Figure 11. Scatter plots of observed monthly precipitation versus predicted precipitation for all months using the CMRM and RK models.

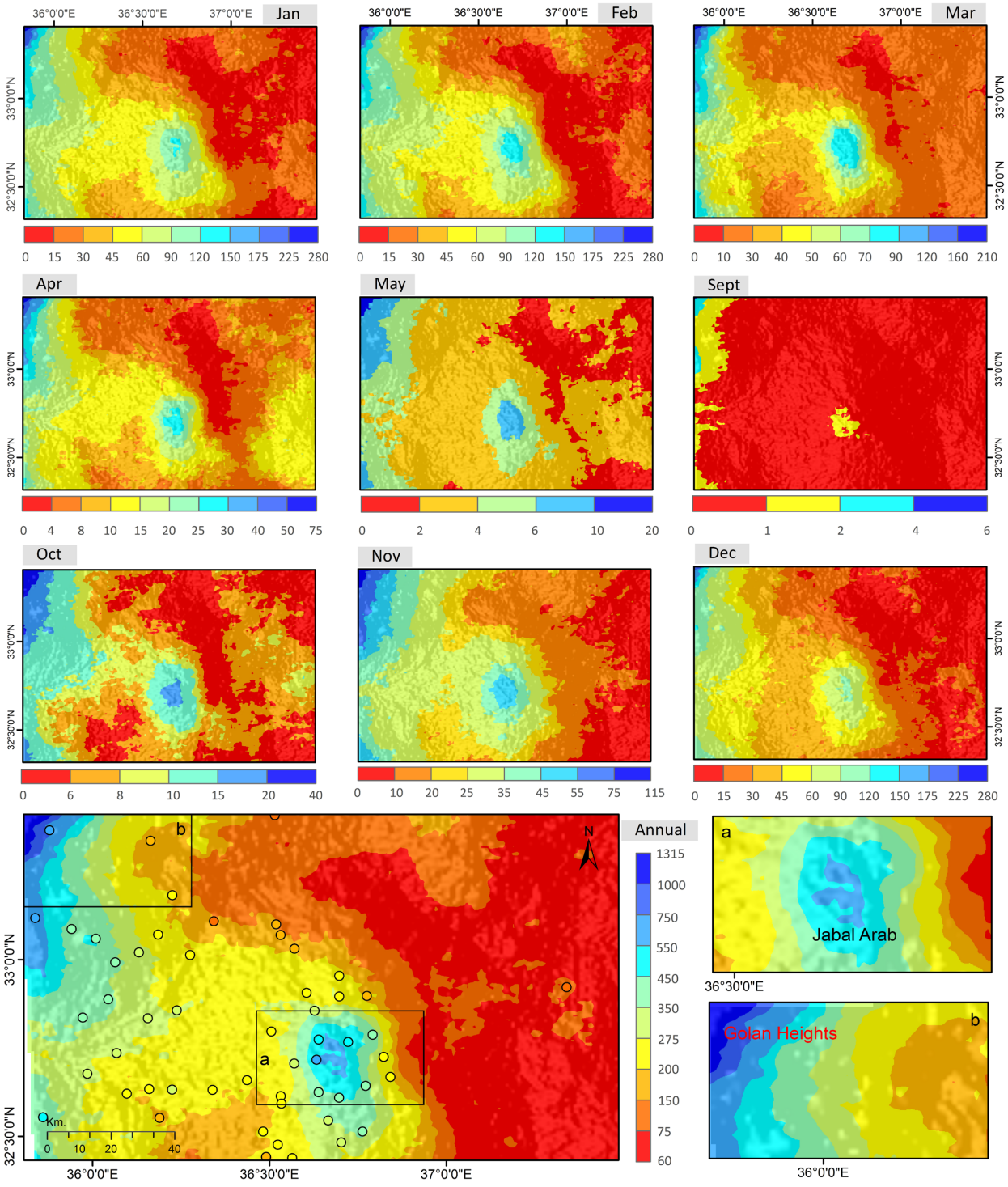


Figure 12. Final monthly precipitation models using the RK method at ~1 km resolution.

For a more detailed evaluation of the performance of the proposed models, the predicted precipitation surfaces by the models were compared with WorldCim, CHELSA, and TerraClimate monthly precipitation surfaces using the Taylor diagram. The results show that the single and hybrid models are better than the global models, indicating the high efficiency of the models. The WorldClim and TerraClimate show an r of 0.92, while the CHELSA shows a low accuracy with an r of 0.8 (Figure 13).

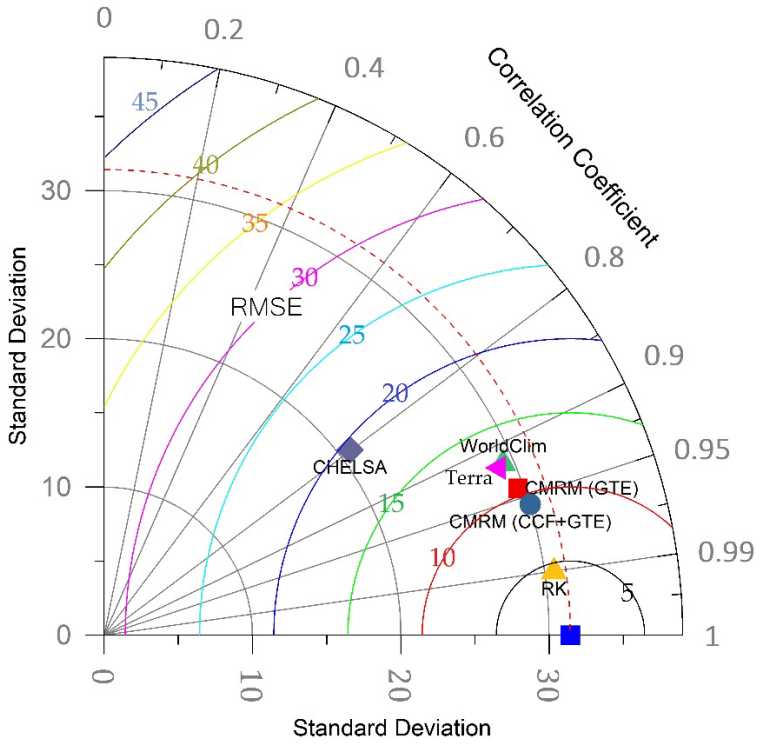


Figure 13. Taylor diagram showing the performance of the models against WorldCim, CHELSA, and TerraClimate monthly precipitation surfaces.

4. Discussion

Precipitation is one of the crucial hydrological and meteorological factors that varies complexly in space and time. Knowledge about spatial precipitation patterns is key for understanding the changes in climate and hydrology at a global or regional scale [78]. Spatial precipitation pattern is also important for understanding ecosystem production, water-energy balance, and other service sectors. It is critical for meteorological and hydrological monitoring on a daily basis to improve disaster preparedness and water resource management [97–101]. Notably, spatial interpolation of precipitation has become a critical scientific subject of importance in many domains, including hydrology, hydrometeorology, ecology, and biodiversity [102–105]. This study attempted to generate high-resolution precipitation datasets in a complex terrain by employing a hybrid interpolation technique merging conventional multivariate regression modeling and OK. The study considered several physiographic factors as covariates to increase the accuracy of interpolation. The results revealed the technique's ability to replicate monthly precipitation patterns with an adjusted R^2 in the range of 0.75 to 0.96 in different months (pooled R^2 = 0.90). The models' residuals were normally distributed, indicating the model's interpolation capability.

In the literature, many physiographic (elevation, slope, aspect, distance to coast, topographic variability, latitude, and soil type), atmospheric (wind and cloud cover), and biophysical (wetland, land use, and vegetation type) factors have been identified that affect precipitation at regional and global scales [17,18,22,90,106]. These factors interact with each other in complex ways to define spatial variability in precipitation patterns. Therefore, incorporating these factors can improve the accuracy of the interpolation method. The influence of most of these factors mainly depends on the geography and climatic conditions of the region under study [90,107]. However, some factors, such as elevation, cloud cover, and zonal wind, have significant influence on local rainfall variability. In many cases, relevant data on all influencing factors are unavailable, so their proxies are used. For example, distance to a coast is often used as a proxy for wind speed as it usually decreases from the coast to the inland [108]. The present study also found the highest correlation of monthly precipitation with altitude, followed by longitude and distance to the seacoast.

Several studies showed a strong relationship between cloud cover and precipitation [109–111]. For example, Zandi et al. [90] showed the influence of two MODIS cloud properties, cloud fraction and cloud effective radius, on precipitation in Iran's Alborz and Zagros Mountain ranges. Sun et al. [110] showed a strong relationship between cloud-type frequency and precipitation in the United States. These studies suggest using cloud cover data to complement precipitation measurement in areas where rainfall data are scarce. While several studies have demonstrated a strong correlation between cloud cover and precipitation [111,112], the utilization of cloud cover data for interpolating precipitation has been very limited. Karger et al. [22] interpreted global precipitation at 1 km resolution using the MODIS CCF. Zandi et al. [90] employed cloud properties with five more environmental variables for precipitation interpolation over a complex terrain in northwest Iran. Geiss et al. [109] filled in radar precipitation missing data using cloud cover data as a predictor. The present study employed cloud cover data with other physiographic factors to improve precipitation interpolation accuracy. The study showed that incorporation of elevation, latitude, and distance to the seacoast with CCF as covariates significantly improved the interpolation accuracy. Several previous studies also suggested these factors as useful covariates for rainfall interpolation [113–115].

This study showed a high positive correlation between precipitation and elevation. This is because of more precipitation at higher elevations due to orographic lifting and increased condensation at higher altitudes. In contrast, this study revealed a negative relation between precipitation with distance to the coast. This may be due to a negative correlation of distance to the coast with wind speed and cloud cover factor. Doran et al. [116] showed that rainfall-forming clouds are more common in coastal areas than inland. Yincan et al. [117] showed that cloud cover distribution is influenced by wind speed and coastal terrain. The present study also showed the seasonal variability of the correlation with distance to the coast. This is due to the seasonal variability of cloud cover. Prijith et al. [118] showed that cloud cover is generally higher in coastal areas, particularly during summer, suggesting a higher negative correlation. Generally, there is decreasing rainfall with increasing latitude in many regions. However, various factors can influence this relationship, which is not always straightforward [119]. For example, Yu et al. [120] investigated spatial precipitation distribution in the region of the Hengduan Mountains in China with latitude and showed a negative relationship.

The hybridization of multivariate regression and OK provides a flexible and accurate approach for spatial data analysis that can provide an improved representation of spatial patterns [121]. It combines the strengths of both multivariate regression and OK methods to produce more accurate results. It helps overcome the limitations of each method, such as the inability of multivariate regression to account for spatial autocorrelation and the limited ability of OK to capture complex spatial trends [122]. The hybrid technique allows the incorporation of additional spatial information, such as distance and directionality, to better capture spatial patterns in the data. This can result in a more realistic representation of the spatial distribution of the variable of interest [9]. Besides, this method can be tailored to the specific needs of the analysis by adjusting the parameters of the regression model and the kriging interpolation, indicating its greater flexibility [55,123]. Therefore, the hybrid method could replicate monthly precipitation patterns with high adjusted R^2 when it was applied at a regional scale in this study.

5. Conclusions

This study accomplished its primary goal of developing a precise method to obtain continuous precipitation surfaces. This enabled us to integrate statistical tools with spatial interpolation techniques in modeling (multivariate regression with residual correction), resulting in a dataset for monthly precipitation at a fine resolution for a complex terrain. This study used hybrid interpolation techniques and determined the best approach for merging statistical methods (CMRM and PCA) with spatial geostatistical interpolation. As a result, this study and its outputs provide an adequate alternative to applying single

methods and an alternative to using global grid data, which differ from each other in reliability and performance and might have biased outputs. This research contributed to resolving the issue of a shortage of precipitation data, particularly in complicated and distant terrains. The following important points can be summarized for this study:

- The optimal MODIS-CCF surface effects on monthly precipitation patterns are most significant at a horizontal scale of 7 km, and the maximum correlations are in April and March ($r > 0.8$, $p < 0.05$).
- The RK method outperforms the single methods, i.e., the multivariate regression models.
- The geographical and topographical factors can explain 42–70% of the total spatial variance in precipitation. Incorporating CCF as a covariate significantly improves the interpolation accuracy by 5–20%. The kriging of the CMRMs' residuals significantly improves the interpolation accuracy by 12–28%.
- Both the single and the hybrid models are better than the global models (WorldCim, CHELSA, and TerraClimate) in estimating regional precipitation in terms of all statistical indicators.

Obtaining high-quality and high-resolution precipitation data remains very difficult due to the large spatiotemporal variability in precipitation and physical mechanisms. This study offered an objective method to improve interpolation and merge algorithms with remotely sensed data. Nonetheless, this study highlighted a significant problem that may require additional investigation and is a major research hotspot in regional climatic modeling, including enhancing interpolation and integrating approaches to provide regular gridded meteorological data. We strive for an in-depth and holistic evaluation of merging satellite-derived precipitation products with cloud detection and cloud properties (water path, effective particle size, and optical thickness) observed by MODIS, using the observed data to improve interpolation quality. As a result, this field still requires further investigation to improve the accuracy of interpolation before implementing this method using national and/or global datasets.

Author Contributions: Conceptualization, K.A.; methodology, K.A.; software, K.A.; formal analysis, K.A.; investigation, K.A.; data curation, K.A.; writing—original draft preparation, K.A., E.S. and S.S.; writing—review and editing, A.K., S.S., A.A., S.B. and B.B.; visualization, K.A.; supervision, S.B.; funding acquisition, A.A., B.B. and S.B. All authors have read and agreed to the published version of the manuscript.

Funding: This work was supported by the National Natural Science Foundation of China (grant numbers 41971340 and 41271410), and also was supported by the Researchers Supporting Project (grant number RSP2023R296), King Saud University, Riyadh, Saudi Arabia.

Data Availability Statement: Not applicable.

Conflicts of Interest: The authors declare no conflict of interest.

References

1. Alsafadi, K.; Mohammed, S.; Habib, H.; Kiwan, S.; Hennawi, S.; Sharaf, M. An Integration of Bioclimatic, Soil, and Topographic Indicators for Viticulture Suitability Using Multi-Criteria Evaluation: A Case Study in the Western Slopes of Jabal Al Arab—Syria. *Geocarto Int.* **2020**, *35*, 1466–1488. [CrossRef]
2. Moreira, R.M.; dos Santos, B.C.; Sanches, R.G.; Bourscheidt, V.; de Sales, F.; Sieber, S.; de Souza, P.H. Precipitation Variability for Protected Areas of Primary Forest and Pastureland in Southwestern Amazônia. *Climate* **2023**, *11*, 27. [CrossRef]
3. Ray, R.L.; Sishodia, R.P.; Tefera, G.W. Evaluation of Gridded Precipitation Data for Hydrologic Modeling in North-Central Texas. *Remote Sens.* **2022**, *14*, 3860. [CrossRef]
4. Ly, S.; Charles, C.; Degré, A. Geostatistical Interpolation of Daily Rainfall at Catchment Scale: The Use of Several Variogram Models in the Ourthe and Ambleve Catchments, Belgium. *Hydrol. Earth Syst. Sci.* **2011**, *15*, 2259–2274. [CrossRef]
5. Durre, I.; Arguez, A.; Schreck, C.J.; Squires, M.F.; Vose, R.S. Daily High-Resolution Temperature and Precipitation Fields for the Contiguous United States from 1951 to Present. *J. Atmos. Ocean. Technol.* **2022**, *39*, 1837–1855. [CrossRef]
6. Sun, R.; Zhang, B.P.; Tan, J. A Multivariate Regression Model for Predicting Precipitation in the Daqing Mountains. *Mt. Res. Dev.* **2008**, *28*, 318–325. [CrossRef]

7. Kumari, M.; Singh, C.K.; Bakimchandra, O.; Basistha, A. Geographically Weighted Regression Based Quantification of Rainfall-Topography Relationship and Rainfall Gradient in Central Himalayas. *Int. J. Climatol.* **2017**, *37*, 1299–1309. [CrossRef]
8. Arowolo, A.O.; Bhowmik, A.K.; Qi, W.; Deng, X. Comparison of spatial interpolation techniques to generate high-resolution climate surfaces for Nigeria. *Int. J. Climatol.* **2017**, *37*, 179–192. [CrossRef]
9. Hu, Q.; Li, Z.; Wang, L.; Huang, Y.; Wang, Y.; Li, L. Rainfall Spatial Estimations: A Review from Spatial Interpolation to Multi-Source Data Merging. *Water* **2019**, *11*, 579. [CrossRef]
10. New, M.; Lister, D.; Hulme, M.; Makin, I. A high-resolution data set of surface climate over global land areas. *Clim. Res.* **2002**, *21*, 1–25. [CrossRef]
11. Harris, I.; Jones, P.D.; Osborn, T.J.; Lister, D.H. Updated high-resolution grids of monthly climatic observations–the CRU TS3. 10 Dataset. *Int. J. Climatol.* **2014**, *34*, 623–642. [CrossRef]
12. Kriticos, D.J.; Webber, B.L.; Leriche, A.; Ota, N.; Macadam, I.; Bathols, J.; Scott, J.K. CliMond: Global High-Resolution Historical and Future Scenario Climate Surfaces for Bioclimatic Modelling. *Methods Ecol. Evol.* **2012**, *3*, 53–64. [CrossRef]
13. Fick, S.E.; Hijmans, R.J. WorldClim 2: New 1-km Spatial Resolution Climate Surfaces for Global Land Areas. *Int. J. Climatol.* **2017**, *37*, 4302–4315. [CrossRef]
14. Karger, D.N.; Conrad, O.; Böhner, J.; Kawohl, T.; Kreft, H.; Soria-Auza, R.W.; Zimmermann, N.E.; Linder, H.P.; Kessler, M. Climatologies at high resolution for the earth's land surface areas. *Sci. Data* **2017**, *4*, 170122. [CrossRef]
15. Abatzoglou, J.T.; Dobrowski, S.Z.; Parks, S.A.; Hegewisch, K.C. TerraClimate, a High-Resolution Global Dataset of Monthly Climate and Climatic Water Balance from 1958–2015. *Sci. Data* **2018**, *5*, 170191. [CrossRef]
16. Cuervo-Robayo, A.P.; Téllez-Valdés, O.; Gómez-Albores, M.A.; Venegas-Barrera, C.S.; Manjarrez, J.; Martínez-Meyer, E. An update of high-resolution monthly climate surfaces for Mexico. *Int. J. Climatol.* **2014**, *34*, 2427–2437. [CrossRef]
17. Daly, C.; Halbleib, M.; Smith, J.I.; Gibson, W.P.; Doggett, M.K.; Taylor, G.H.; Curtis, J.; Pasteris, P.P. Physiographically Sensitive Mapping of Climatological Temperature and Precipitation across the Conterminous United States. *Int. J. Climatol.* **2008**, *28*, 2031–2064. [CrossRef]
18. Daly, C.; Slater, M.E.; Roberti, J.A.; Laseter, S.H.; Swift, L.W. High-Resolution Precipitation Mapping in a Mountainous Watershed: Ground Truth for Evaluating Uncertainty in a National Precipitation Dataset. *Int. J. Climatol.* **2017**, *37*, 124–137. [CrossRef]
19. Ninyerola, M.; Pons, X.; Roure, J.M. Monthly Precipitation Mapping of the Iberian Peninsula Using Spatial Interpolation Tools Implemented in a Geographic Information System. *Theor. Appl. Climatol.* **2007**, *89*, 195–209. [CrossRef]
20. Rockel, B. The Regional Downscaling Approach: A Brief History and Recent Advances. *Curr. Clim. Change Rep.* **2015**, *1*, 22–29. [CrossRef]
21. Crespi, A.; Lussana, C.; Brunetti, M.; Dobler, A.; Maugeri, M.; Tveito, O.E. High-resolution monthly precipitation climatologies over Norway (1981–2010): Joining numerical model data sets and in situ observations. *Int. J. Climatol.* **2019**, *39*, 2057–2070. [CrossRef]
22. Karger, D.N.; Wilson, A.M.; Mahony, C.; Zimmermann, N.E.; Jetz, W. Global Daily 1 Km Land Surface Precipitation Based on Cloud Cover-Informed Downscaling. *Sci. Data* **2021**, *8*, 307. [CrossRef] [PubMed]
23. Chen, C.; Chen, Q.; Qin, B.; Zhao, S.; Duan, Z. Comparison of Different Methods for Spatial Downscaling of GPM IMERG V06B Satellite Precipitation Product Over a Typical Arid to Semi-Arid Area. *Front. Earth Sci.* **2020**, *8*, 536337. [CrossRef]
24. Gutmann, E.D.; Rasmussen, R.M.; Liu, C.; Ikeda, K.; Gochis, D.J.; Clark, M.P.; Dudhia, J.; Thompson, G. A Comparison of Statistical and Dynamical Downscaling of Winter Precipitation over Complex Terrain. *J. Clim.* **2012**, *25*, 262–281. [CrossRef]
25. Schneider, R.; Koch, J.; Troldborg, L.; Henriksen, H.J.; Stisen, S. Machine-Learning-Based Downscaling of Modelled Climate Change Impacts on Groundwater Table Depth. *Hydrol. Earth Syst. Sci.* **2022**, *26*, 5859–5877. [CrossRef]
26. Serifi, A.; Günther, T.; Ban, N. Spatio-Temporal Downscaling of Climate Data Using Convolutional and Error-Predicting Neural Networks. *Front. Clim.* **2021**, *3*, 656479. [CrossRef]
27. Wang, F.; Tian, D.; Lowe, L.; Kalin, L.; Lehrter, J. Deep Learning for Daily Precipitation and Temperature Downscaling. *Water Res.* **2021**, *57*, e2020WR029308. [CrossRef]
28. Salimi, A.H.; Masoompour Samakosh, J.; Sharifi, E.; Hassanvand, M.R.; Noori, A.; von Rautenkranz, H. Optimized Artificial Neural Networks-Based Methods for Statistical Downscaling of Gridded Precipitation Data. *Water* **2019**, *11*, 1653. [CrossRef]
29. Coulibaly, M.; Becker, S. Spatial Interpolation of Annual Precipitation in South Africa-Comparison and Evaluation of Methods. *Water Int.* **2007**, *32*, 494–502. [CrossRef]
30. Chutsagulprom, N.; Chaisee, K.; Wongsaijai, B.; Inkeaw, P.; Oonariya, C. Spatial Interpolation Methods for Estimating Monthly Rainfall Distribution in Thailand. *Theor. Appl. Climatol.* **2022**, *148*, 317–328. [CrossRef]
31. Vargas-Guzman, J.A.; Warrick, A.W. *Geostatistics for Natural Resources Evaluation: Pierre Goovaerts*; Oxford University Press: Madison Avenue, NY, USA, 1997; 483p, ISBN 0-19-511538-4.
32. Ahrens, B. Distance in Spatial Interpolation of Daily Rain Gauge Data. *Hydrol. Earth Syst. Sci.* **2006**, *10*, 197–208. [CrossRef]
33. Goovaerts, P. Geostatistical approaches for incorporating elevation into the spatial interpolation of rainfall. *J. Hydrol.* **2000**, *228*, 113–129. [CrossRef]
34. Feki, H.; Slimani, M.; Cudennec, C. Incorporating elevation in rainfall interpolation in Tunisia using geostatistical methods. *Hydrol. Sci. J.* **2012**, *57*, 1294–1314. [CrossRef]
35. Adhikary, S.K.; Muttil, N.; Yilmaz, A.G. Cokriging for Enhanced Spatial Interpolation of Rainfall in Two Australian Catchments. *Hydrol. Process.* **2017**, *31*, 2143–2161. [CrossRef]

36. Li, J.; Heap, A.D. A Review of Comparative Studies of Spatial Interpolation Methods in Environmental Sciences: Performance and Impact Factors. *Ecol. Inform.* **2011**, *6*, 228–241. [CrossRef]
37. Herrera, S.; Kotlarski, S.; Soares, P.M.M.; Cardoso, R.M.; Jaczewski, A.; Gutiérrez, J.M.; Maraun, D. Uncertainty in Gridded Precipitation Products: Influence of Station Density, Interpolation Method and Grid Resolution. *Int. J. Climatol.* **2019**, *39*, 3717–3729. [CrossRef]
38. Bostan, P.A.; Heuvelink, G.B.M.; Akyurek, S.Z. Comparison of Regression and Kriging Techniques for Mapping the Average Annual Precipitation of Turkey. *Int. J. Appl. Earth Obs. Geoinf.* **2012**, *19*, 115–126. [CrossRef]
39. Brunsdon, C.; McClatchey, J.; Unwin, D.J. Spatial Variations in the Average Rainfall-Altitude Relationship in Great Britain: An Approach Using Geographically Weighted Regression. *Int. J. Climatol.* **2001**, *21*, 455–466. [CrossRef]
40. Lloyd, C. Nonstationary models for exploring and mapping monthly precipitation in the United Kingdom. *Int. J. Climatol.* **2010**, *30*, 390–405. [CrossRef]
41. Kumari, M.; Singh, C.K.; Basistha, A.; Dorji, S.; Tamang, T.B. Nonstationary modelling framework for rainfall interpolation in complex terrain. *Int. J. Climatol.* **2017**, *37*, 4171–4185. [CrossRef]
42. Aalto, J.; Pirinen, P.; Heikkinen, J.; Venäläinen, A. Spatial Interpolation of Monthly Climate Data for Finland: Comparing the Performance of Kriging and Generalized Additive Models. *Theor. Appl. Climatol.* **2013**, *112*, 99–111. [CrossRef]
43. Brunsdon, C.; Fotheringham, A.S.; Charlton, M.E. Geographically Weighted Regression: A Method for Exploring Spatial Nonstationarity. *Geogr. Anal.* **1996**, *28*, 281–298. [CrossRef]
44. Brunsdon, C.; Fotheringham, A.S.; Charlton, M. Geographically Weighted Summary Statistics—A Framework for Localised Exploratory Data Analysis. *Comput. Environ. Urban Syst.* **2002**, *26*, 501–524. [CrossRef]
45. Huang, B.; Wu, B.; Barry, M. Geographically and Temporally Weighted Regression for Modeling Spatio-Temporal Variation in House Prices. *Int. J. Geogr. Inf. Sci.* **2010**, *24*, 383–401. [CrossRef]
46. Papacharalampous, G.; Tyralis, H.; Doulamis, A.; Doulamis, N. Comparison of Machine Learning Algorithms for Merging Gridded Satellite and Earth-Observed Precipitation Data. *Water* **2023**, *15*, 634. [CrossRef]
47. Rigol, J.P.; Jarvis, C.H.; Stuart, N. Artificial Neural Networks as a Tool for Spatial Interpolation. *Int. J. Geogr. Inf. Sci.* **2001**, *15*, 323–343. [CrossRef]
48. Kalteh, A.M.; Berndtsson, R. Interpolating Monthly Precipitation by Self-Organizing Map (SOM) and Multilayer Perceptron (MLP). *Hydrol. Sci. J.* **2007**, *52*, 305–317. [CrossRef]
49. Kajornrit, J.; Wong, K.W.; Fung, C.C. An Interpretable Fuzzy Monthly Rainfall Spatial Interpolation System for the Construction of Aerial Rainfall Maps. *Soft Comput.* **2016**, *20*, 4631–4643. [CrossRef]
50. Hengl, T.; Nussbaum, M.; Wright, M.N.; Heuvelink, G.B.; Gräler, B. Random forest as a generic framework for predictive modeling of spatial and spatio-temporal variables. *PeerJ* **2018**, *6*, e5518. [CrossRef]
51. Sekulić, A.; Kilibarda, M.; Heuvelink, G.B.M.; Nikolić, M.; Bajat, B. Random Forest Spatial Interpolation. *Remote Sens.* **2020**, *12*, 1687. [CrossRef]
52. Chen, C.; Hu, B.; Li, Y. Easy-to-Use Spatial Random-Forest-Based Downscaling-Calibration Method for Producing Precipitation Data with High Resolution and High Accuracy. *Hydrol. Earth Syst. Sci.* **2021**, *25*, 5667–5682. [CrossRef]
53. Pour, S.H.; Shahid, S.; Chung, E.S. A hybrid model for statistical downscaling of daily rainfall. *Procedia Eng.* **2016**, *154*, 1424–1430. [CrossRef]
54. Sharifi, E.; Saghafian, B.; Steinacker, R. Copula-Based Stochastic Uncertainty Analysis of Satellite Precipitation Products. *J. Hydrol.* **2019**, *570*, 739–754. [CrossRef]
55. Álvarez-Rodríguez, J.; Llasat, M.C.; Estrela, T. Development of a Hybrid Model to Interpolate Monthly Precipitation Maps Incorporating the Orographic Influence. *Int. J. Climatol.* **2019**, *39*, 3962–3975. [CrossRef]
56. Zhang, W.; Liu, D.; Zheng, S.; Liu, S.; Loáiciga, H.A.; Li, W. Regional Precipitation Model Based on Geographically and Temporally Weighted Regression Kriging. *Remote Sens.* **2020**, *12*, 2547. [CrossRef]
57. Alsafadi, K.; Mohammed, S.; Mokhtar, A.; Sharaf, M.; He, H. Fine-Resolution Precipitation Mapping over Syria Using Local Regression and Spatial Interpolation. *Atmos. Res.* **2021**, *256*, 105524. [CrossRef]
58. Guan, H.; Hsu, H.H.; Makhnin, O.; Xie, H.; Wilson, J.L. Examination of Selected Atmospheric and Orographic Effects on Monthly Precipitation of Taiwan Using the ASOADeK Model. *Int. J. Climatol.* **2009**, *29*, 1171–1181. [CrossRef]
59. Guan, H.; Wilson, J.L.; Makhnin, O. Geostatistical Mapping of Mountain Precipitation Incorporating Autosearched Effects of Terrain and Climatic Characteristics. *J. Hydrometeorol.* **2005**, *6*, 1018–1031. [CrossRef]
60. Odeh, I.O.A.; McBratney, A.B.; Chittleborough, D.J. Further Results on Prediction of Soil Properties from Terrain Attributes: Heterotopic Cokriging and Regression-Kriging. *Geoderma* **1995**, *67*, 215–226. [CrossRef]
61. Hengl, T.; Heuvelink, G.B.M.; Rossiter, D.G. About Regression-Kriging: From Equations to Case Studies. *Comput. Geosci.* **2007**, *33*, 1301–1315. [CrossRef]
62. Sun, W.; Zhu, Y.; Huang, S.; Guo, C. Mapping the Mean Annual Precipitation of China Using Local Interpolation Techniques. *Theor. Appl. Climatol.* **2014**, *119*, 171–180. [CrossRef]
63. Seo, Y.; Kim, S.; Singh, V.P. Estimating spatial precipitation using regression kriging and artificial neural network residual kriging (RKNNRK) hybrid approach. *Water Resour. Manag.* **2015**, *29*, 2189–2204. [CrossRef]
64. Kisi, O.; Mohsenzadeh Karimi, S.; Shiri, J.; Keshavarzi, A. Modelling long-term monthly rainfall using geographical inputs: Assessing heuristic and geostatistical models. *Meteorol. Appl.* **2019**, *26*, 698–710. [CrossRef]

65. Lei, J.; Quan, Q.; Li, P.; Yan, D. Research on monthly precipitation prediction based on the least square support vector machine with multi-factor integration. *Atmosphere* **2021**, *12*, 1076. [CrossRef]
66. Tan, J.; Xie, X.; Zuo, J.; Xing, X.; Liu, B.; Xia, Q.; Zhang, Y. Coupling random forest and inverse distance weighting to generate climate surfaces of precipitation and temperature with multiple-covariates. *J. Hydrol.* **2021**, *598*, 126270. [CrossRef]
67. Brunetti, M.; Maugeri, M.; Nanni, T.; Simolo, C.; Spinoni, J. High-resolution temperature climatology for Italy: Interpolation method intercomparison. *Int. J. Climatol.* **2014**, *34*, 1278–1296. [CrossRef]
68. Wang, M.; He, G.; Zhang, Z.; Wang, G.; Zhang, Z.; Cao, X.; Wu, Z.; Liu, X. Comparison of spatial interpolation and regression analysis models for an estimation of monthly near surface air temperature in China. *Remote Sens.* **2017**, *9*, 1278. [CrossRef]
69. Cristóbal, J.; Ninyerola, M.; Pons, X. Modeling air temperature through a combination of remote sensing and GIS data J. *Geophys. Res. Atmos.* **2008**, *113*, D13106. [CrossRef]
70. Antal, A.; Guerreiro, P.M.; Cheval, S. Comparison of spatial interpolation methods for estimating the precipitation distribution in Portugal. *Theor. Appl. Climatol.* **2021**, *145*, 1193–1206. [CrossRef]
71. Immerzeel, W.W.; Rutten, M.M.; Droogers, P. Spatial downscaling of TRMM precipitation using vegetative response on the Iberian Peninsula. *Remote Sens. Environ.* **2009**, *113*, 362–370. [CrossRef]
72. Jia, S.; Zhu, W.; Lű, A.; Yan, T. A statistical spatial downscaling algorithm of TRMM precipitation based on NDVI and DEM in the Qaidam Basin of China. *Remote Sens. Environ.* **2011**, *115*, 3069–3079. [CrossRef]
73. Lu, X.; Tang, G.; Wang, X.; Liu, Y.; Wei, M.; Zhang, Y. The development of a two-step merging and downscaling method for satellite precipitation products. *Remote Sens.* **2020**, *12*, 398. [CrossRef]
74. Cheema, M.J.M.; Bastiaanssen, W.G.M.; Rutten, M.M. Validation of surface soil moisture from AMSR-E using auxiliary spatial data in the transboundary Indus Basin. *J. Hydrol.* **2011**, *405*, 137–149. [CrossRef]
75. Richards, F.; Arkin, P. On the relationship between satellite-observed cloud cover and precipitation. *Mon. Weather Rev.* **1981**, *109*, 1081–1093. [CrossRef]
76. Arkin, P.A.; Meisner, B.N. The relationship between large-scale convective rainfall and cold cloud over the western hemisphere during 1982–84. *Mon. Weather Rev.* **1987**, *115*, 51–74. [CrossRef]
77. Betts, A.K.; Tawfik, A.B.; Desjardins, R.L. Revisiting Hydrometeorology Using Cloud and Climate Observations. *J. Hydrometeorol.* **2017**, *18*, 939–955. [CrossRef]
78. Alsafadi, K.; Bi, S.; Abdo, H.G.; Almohamad, H.; Alatrach, B.; Srivastava, A.K.; Al-Mutiry, M.; Bal, S.K.; Chandran, M.A.S.; Mohammed, S. Modeling the Impacts of Projected Climate Change on Wheat Crop Suitability in Semi-Arid Regions Using the AHP-Based Weighted Climatic Suitability Index and CMIP6. *Geosci. Lett.* **2023**, *10*, 20. [CrossRef]
79. Wilson, A.M.; Jetz, W. Remotely sensed high-resolution global cloud dynamics for predicting ecosystem and biodiversity distributions. *PLoS Biol.* **2016**, *14*, e1002415. [CrossRef]
80. Danielson, J.J.; Gesch, D.B. *Global Multi-Resolution Terrain Elevation Data 2010 (GMTED2010)*; US Department of the Interior, US Geological Survey: Reston, VA, USA, 2011; p. 101. 26p.
81. Alexandersson, H. A homogeneity test applied to precipitation data. *J. Climatol.* **1986**, *6*, 661–675. [CrossRef]
82. Štěpánek, P.; Zahradníček, P.; Skalák, P. Data quality control and homogenization of air temperature and precipitation series in the area of the Czech Republic in the period 1961–2007. *Adv. Sci. Res.* **2009**, *3*, 23–26. [CrossRef]
83. Zhu, X.; Qiu, X.; Zeng, Y.; Ren, W.; Tao, B.; Pan, H.; Gao, T.; Gao, J. High-resolution precipitation downscaling in mountainous areas over China: Development and application of a statistical mapping approach. *Int. J. Climatol.* **2018**, *38*, 77–93. [CrossRef]
84. Daly, C.; Smith, J.W.; Smith, J.I.; McKane, R.B. High-Resolution Spatial Modeling of Daily Weather Elements for a Catchment in the Oregon Cascade Mountains, United States. *J. Appl. Meteorol. Climatol.* **2007**, *46*, 1565–1586. [CrossRef]
85. Portalés, C.; Boronat, N.; Pardo-Pascual, J.E.; Balaguer-Beser, A. Seasonal precipitation interpolation at the Valencia region with multivariate methods using geographic and topographic information. *Int. J. Climatol.* **2010**, *30*, 1547–1563. [CrossRef]
86. Qi, W.W.; Zhang, B.P.; Yao, Y.H.; Zhao, F.; Zhang, S.; He, W.H. A topographical model for precipitation pattern in the Tibetan Plateau. *J. Mt. Sci.* **2016**, *13*, 763–773. [CrossRef]
87. Drogue, G.; Humbert, J.; Deraisme, J.; Mahr, N.; Freslon, N. A statistical–topographic model using an omnidirectional parameterization of the relief for mapping orographic rainfall. *Int. J. Climatol.* **2002**, *22*, 599–613. [CrossRef]
88. Lloyd, C. Assessing the effect of integrating elevation data into the estimation of monthly precipitation in Great Britain. *J. Hydrol.* **2005**, *308*, 128–150. [CrossRef]
89. Sharifi, E.; Saghafian, B.; Steinacker, R. Downscaling Satellite Precipitation Estimates with Multiple Linear Regression, Artificial Neural Networks, and Spline Interpolation Techniques. *J. Geophys. Res. Atmos.* **2019**, *124*, 789–805. [CrossRef]
90. Zandi, O.; Zahraie, B.; Nasseri, M.; Behrangi, A. Stacking machine learning models versus a locally weighted linear model to generate high-resolution monthly precipitation over a topographically complex area. *Atmos. Res.* **2022**, *272*, 106159. [CrossRef]
91. Bartholomew, D.J. *Principal Components Analysis*, 3rd ed.; Peterson, P., Baker, E., McGaw, B., Eds.; Elsevier: Oxford, UK, 2010; pp. 374–377. [CrossRef]
92. Abdi, H.; Williams, L.J. Principal component analysis. *WIREs Comput. Stat.* **2010**, *2*, 433–459. [CrossRef]
93. Sulaiman, M.S.; Abood, M.M.; Sinnakaudan, S.K.; Shukor, M.R.; You, G.Q.; Chung, X.Z. Assessing and solving multicollinearity in sediment transport prediction models using principal component analysis. *ISH J. Hydraul. Eng.* **2021**, *27* (Suppl. 1), 343–353. [CrossRef]

94. Chen, T.; Ren, L.; Yuan, F.; Yang, X.; Jiang, S.; Tang, T.; Liu, Y.; Zhao, C.; Zhang, L. Comparison of Spatial Interpolation Schemes for Rainfall Data and Application in Hydrological Modeling. *Water* **2017**, *9*, 342. [CrossRef]
95. Abreu, M.C.; de Souza, A.; Lyra, G.B.; Pobocikova, I.; Cecílio, R.A. Analysis of Monthly and Annual Rainfall Variability Using Linear Models in the State of Mato Grosso Do Sul, Midwest of Brazil. *Int. J. Climatol.* **2021**, *41*, E2445–E2461. [CrossRef]
96. Tveito, O.E.; Wegehenkel, M.; Wel, F.V.D. The use of geographic information systems in climatology and meteorology. In *Cost Action 719*; EU Publications: Luxembourg, 2008. [CrossRef]
97. Faurès, J.M.; Goodrich, D.C.; Woolhiser, D.A.; Sorooshian, S. Impact of small-scale spatial rainfall variability on runoff modeling. *J. Hydrol.* **1995**, *173*, 309–326. [CrossRef]
98. Michaelides, S.C.; Tymvios, F.S.; Michaelidou, T. Spatial and temporal characteristics of the annual rainfall frequency distribution in Cyprus. *Atmos. Res.* **2009**, *94*, 606–615. [CrossRef]
99. Elbeltagi, A.; Kumari, N.; Dharpure, J.K.; Mokhtar, A.; Alsafadi, K.; Kumar, M.; Mehdinejadiani, B.; Ramezani Etedali, H.; Brouziyne, Y.; Towfiqul Islam, A.R.M.; et al. Prediction of combined terrestrial evapotranspiration index (CTEI) over large river basin based on machine learning approaches. *Water* **2021**, *13*, 547. [CrossRef]
100. Mokhtar, A.; Jalali, M.; He, H.; Al-Ansari, N.; Elbeltagi, A.; Alsafadi, K.; Abdo, H.G.; Sammen, S.S.; Gyasi-Agyei, Y.; Rodrigo-Comino, J. Estimation of SPEI meteorological drought using machine learning algorithms. *IEEE Access* **2021**, *9*, 65503–65523. [CrossRef]
101. Li, X.; He, X.; Li, X.; Du, Y.; Yang, G.; Tian, H.; Yu, J. Construction of high-resolution precipitation dataset and its implication to drought over the Tianshan Mountains, China. *Front. Earth Sci.* **2023**, *11*, 1128990. [CrossRef]
102. Hong, Y.; Adler, R.; Huffman, G. Evaluation of the potential of NASA multi-satellite precipitation analysis in global landslide hazard assessment. *Geophys. Res. Lett.* **2006**, 33. [CrossRef]
103. Ceron, W.L.; Andreoli, R.V.; Kayano, M.T.; Canchala, T.; Carvajal-Escobar, Y.; Souza, R.A. Comparison of spatial interpolation methods for annual and seasonal rainfall in two hotspots of biodiversity in South America. *An. Acad. Bras. Cienc.* **2021**, *93*, e20190674. [CrossRef]
104. Alsafadi, K.; Bi, S.; Abdo, H.G.; Al Sayah, M.J.; Ratonyi, T.; Harsanyi, E.; Mohammed, S. Spatial–temporal dynamic impact of changes in rainfall erosivity and vegetation coverage on soil erosion in the Eastern Mediterranean. *Environ. Sci. Pollut. Res.* **2022**, 1–19. [CrossRef]
105. Huang, Z.; Derin, Y.; Kirstetter, P.E.; Li, Y. Multigraph Convolutional Networks for Rainfall Estimation in Complex Terrain. *EEE Geosci. Remote Sens. Lett.* **2022**, *19*, 1506005. [CrossRef]
106. Kumar, A.; Kumar, M.; Pandey, R.; ZhiGuo, Y.; Cabral-Pinto, M. Forest Soil Nutrient Stocks along Altitudinal Range of Uttarakhand Himalayas: An Aid to Nature Based Climate Solutions. *Catena* **2021**, *207*, 105667. [CrossRef]
107. Bhardwaj, D.R.; Tahiry, H.; Sharma, P.; Pala, N.A.; Kumar, D.; Kumar, A.; Bharti. Influence of Aspect and Elevational Gradient on Vegetation Pattern, Tree Characteristics and Ecosystem Carbon Density in Northwestern Himalayas. *Land* **2021**, *10*, 1109. [CrossRef]
108. Camera, C.; Bruggeman, A.; Hadjinicolaou, P.; Pashiardis, S.; Lange, M.A. Evaluation of interpolation techniques for the creation of gridded daily precipitation (1×1 km^2); Cyprus, 1980–2010. *J. Geophys. Res. Atmos.* **2014**, *119*, 693–712. [CrossRef]
109. Geiss, A.; Hardin, J.C. Inpainting Radar Missing Data Regions with Deep Learning. *Atmos. Meas. Tech.* **2021**, *14*, 7729–7747. [CrossRef]
110. Sun, B.; Groisman, P.Y.; Mokhov, I.I. Recent changes in cloud-type frequency and inferred increases in convection over the United States and the former USSR. *J. Clim.* **2001**, *14*, 1864–1880. [CrossRef]
111. Mishra, A.K. Investigating changes in cloud cover using the long-term record of precipitation extremes. *Meteorol. Appl.* **2019**, *26*, 108–116. [CrossRef]
112. Zhong, X.; Liu, S.C.; Liu, R.; Wang, X.; Mo, J.; Li, Y. Observed trends in clouds and precipitation (1983–2009): Implications for their cause(s). *Atmos. Chem. Phys.* **2021**, *21*, 4899–4913. [CrossRef]
113. Hijmans, R.J.; Cameron, S.E.; Parra, J.L.; Jones, P.G.; Jarvis, A. Very high resolution interpolated climate surfaces for global land areas. *Int. J. Climatol.* **2005**, *25*, 1965–1978. [CrossRef]
114. Dewan, A.; Shahid, S.; Bhuian, M.H.; Hossain, S.M.J.; Nashwan, M.S.; Chung, E.S.; Hassan, Q.K.; Asaduzzaman, M. Developing a high-resolution gridded rainfall product for Bangladesh during 1901–2018. *Sci. Data* **2022**, *9*, 471. [CrossRef]
115. Pellicone, G.; Caloiero, T.; Modica, G.; Guagliardi, I. Application of several spatial interpolation techniques to monthly rainfall data in the Calabria region (southern Italy). *Int. J. Climatol.* **2018**, *38*, 3651–3666. [CrossRef]
116. Doran, J.C.; Zhong, S.; Liljegren, J.C.; Jakob, C. A comparison of cloud properties at a coastal and inland site at the North Slope of Alaska. *J. Geophys. Res. Atmos.* **2002**, *107*, ACL-5. [CrossRef]
117. Ye, Y. Marine Geographic and Geological Environment of China. *Mar. Geo-Hazards China* **2017**, *10*, 35–75. [CrossRef]
118. Prijith, S.S.; Lima, C.B.; Ramana, M.V.; Sai, M.S. Intra-seasonal contrasting trends in clouds due to warming induced circulation changes. *Sci. Rep.* **2021**, *11*, 16985. [CrossRef]
119. Pielke Sr, R.A.; Adegoke, J.; BeltraáN-Przekurat, A.; Hiemstra, C.A.; Lin, J.; Nair, U.S.; Niyogi, D.; Nobis, T.E. An overview of regional land-use and land-cover impacts on rainfall. *Tellus B Chem. Phys. Meteorol.* **2007**, *59*, 587–601. [CrossRef]
120. Yu, H.; Wang, L.; Yang, R.; Yang, M.; Gao, R. Temporal and spatial variation of precipitation in the Hengduan Mountains region in China and its relationship with elevation and latitude. *Atmos. Res.* **2018**, *213*, 1–16. [CrossRef]

121. Meng, Q.; Liu, Z.; Borders, B.E. Assessment of Regression Kriging for Spatial Interpolation—Comparisons of Seven GIS Interpolation Methods. *Cartogr. Geogr. Inf. Sci.* **2013**, *40*, 28–39. [CrossRef]
122. Mishra, P.K.; Nath, S.K.; Sen, M.K.; Fasshauer, G.E. Hybrid Gaussian-cubic radial basis functions for scattered data interpolation. *Comput. Geosci.* **2018**, *22*, 1203–1218. [CrossRef]
123. Khedhaouiria, D.; Bélair, S.; Fortin, V.; Roy, G.; Lespinas, F. Using a hybrid optimal interpolation–ensemble Kalman filter for the Canadian Precipitation Analysis. *Nonlinear Process. Geophys.* **2022**, *29*, 329–344. [CrossRef]

Disclaimer/Publisher's Note: The statements, opinions and data contained in all publications are solely those of the individual author(s) and contributor(s) and not of MDPI and/or the editor(s). MDPI and/or the editor(s) disclaim responsibility for any injury to people or property resulting from any ideas, methods, instructions or products referred to in the content.